



Diploma thesis

Beam diagnostics and analysis of the optical properties of the MAMI beam delivery system

Marco Dehn

May 2004

Table of contents

I. Introduction	5
1. Mainz Microtron MAMI	6
II. Beam optics	7
2. Beam optical measurement	8
2.1. Matrix formalism	8
2.1.1. Drift track	11
2.1.2. Dipole	11
2.1.3. Quadrupole	13
2.2. Principle of measurement	14
2.2.1. Procedure for determining the matrix elements	14
2.3. Measuring routine	16
2.3.1. Input parameters before starting a measurement	16
2.3.2. Input parameters before each measurement series	17
2.3.3. One measuring cycle	17
2.4. Optical settings	17
2.5. Evaluation	19
2.5.1. Setting up the matrix	19
2.5.2. Error analysis	19
2.6. Result: Adaptation of the model	21
III. Radiation diagnostics	23
3. HF position monitors	24
3.1. Basics of HF position monitors	24
3.2. Structure of the xy-monitor <i>system</i>	25
3.2.1. The <i>xy</i> monitor	25
3.2.2. The measurement electronics	26
3.2.3. Calibration of the measuring electronics	26
3.3. Measurements with beam	29
3.4. Non-linearity of the sensitivity of the xy-monitor	34

4. Calibration of an HF position monitor	37
4.1. The lifting mechanism	37
4.1.1. Principle of the lifting mechanism	38
4.1.2. Calibration of the lifting mechanism.....	41
4.1.3. Bending of the tapered threaded bolts	42
4.1.4. Load on the gearbox	43
4.1.5. Engine power	44
4.2. Calibration of the signals during beam operation.....	45
4.2.1. Setting the reference phase	45
4.2.2. Calibration with c.w. beam.....	45
4.2.3. Calibration with diagnostic pulses.....	45
5. COBRA multiplexer	48
5.1. Introduction to the previous system	48
5.2. Technical parameters	50
5.2.1. Control of the multiplexer	50
5.2.2. Triggering the oscilloscope	50
5.3. Jitter study.....	52
5.4. Structure of the COBRA add-on module	53
5.4.1. Hardware.....	53
5.4.2. Software.....	53
5.5. The result	55
6. Summary	56
6.1. Beam optical measurement	56
6.2. HF position monitors.....	56
6.3. The COBRA Multiplexer	57
Acknowledgement	58
IV. Appendix	59
1. Correction magnets	60
1.1. Compilation of the most important data.....	62
2. Quadrupole	64
2.1. Simple check of the strength of a quadrupole	64
2.1.1. Point-to-point mapping	64
3. Theory of HF monitors (by H. Herminghaus)	68
3.1. Fields in cylindrical waveguides.....	68
3.2. Standing waves in resonators.....	69
3.3. The relativistic particle in the HF field	70
3.4. Rotationally symmetric resonators	71

Part I.

Introduction

1st Mainz Microtron MAMI

Since 1990, the Institute of Nuclear Physics has been operating the Mainz microtron MAMI B for nuclear physics experiments and tests on the generation and application of coherent radiation, which delivers a continuous beam of electrons up to a maximum energy of 855 MeV.

About the work

The aim of this work is to improve beam diagnostics in the beam delivery system from the accelerator to the experimental halls and to analyse the optical properties of a section of this system. For this purpose, an apparatus was developed which allows an accurate calibration of RF beam position monitors during beam operation.

In addition, in order to shorten the setting times and to simplify the monitoring of the beam positions in the transport systems, a circuit was developed on the basis of a microprocessor system that enables the display of several such monitors apparently simultaneously.

The appendix describes the measurement of the correction magnets used. In addition, the theory of HF monitors, which was described in various lectures at the Institute, is presented there in a summary.

Part II.

Beam optics

2. beam optical measurement

The beam guidance system downstream of the accelerator is intended to transport the electron beam to the respective experiment site without loss and with the focus required by the experiment. For this purpose, it consists of various subsections which have been dimensioned as far as possible with regard to simple and manageable transformation properties. As a rule, the individual deflection systems should be achromatic and behave like simple drift paths.

The actual beam focusing is carried out with the aid of quadrupole lenses located between the sections. With the help of such an arrangement, it is possible to adapt to the beam properties that depend on the output energy and to react flexibly to different requirements of the experiments.

Due to setting uncertainties in quadrupoles and unknown field inhomogeneities in the deflection dipoles, however, the actual behaviour of the deflection systems deviates to a greater or lesser extent from the respective concept and thus causes difficulties in beam setting.

The aim of this work was to investigate the possibility of determining the imaging properties as reliably as possible with the aid of the electron beam. The second half of the transfer system converted in the course of the conversion for MAMI C in 2001 (referred to as the T2 system in the following) was chosen as an example, since there is sufficient space in *front of* this section for two small correction magnets and several HF position monitors are available *behind it*.

To measure the beam guidance, the position and direction of the electron beam at the input of the section to be measured were varied in a defined manner with these wedlers and the position and direction changes were measured in HF position monitors at the output.

In principle, nearby light screens could also have been used for this purpose. The disadvantage here, however, would be that the position of the beam could only be read with an accuracy of 0.1 mm and this procedure could not be used in a simple, automated way. In contrast, HF position monitors provide signals that can be easily digitised and can thus be used in an automatic measurement routine.

2.1. Matrix formalism

The investigation of the beam optics was based on the matrix calculation, which describes the relationship between the input and output coordinates a_1 and a_n *of* a particle as it passes through an optical system with n elements in a linear approximation. The position and momentum of a particle are determined by specifying its phase space coordinates.

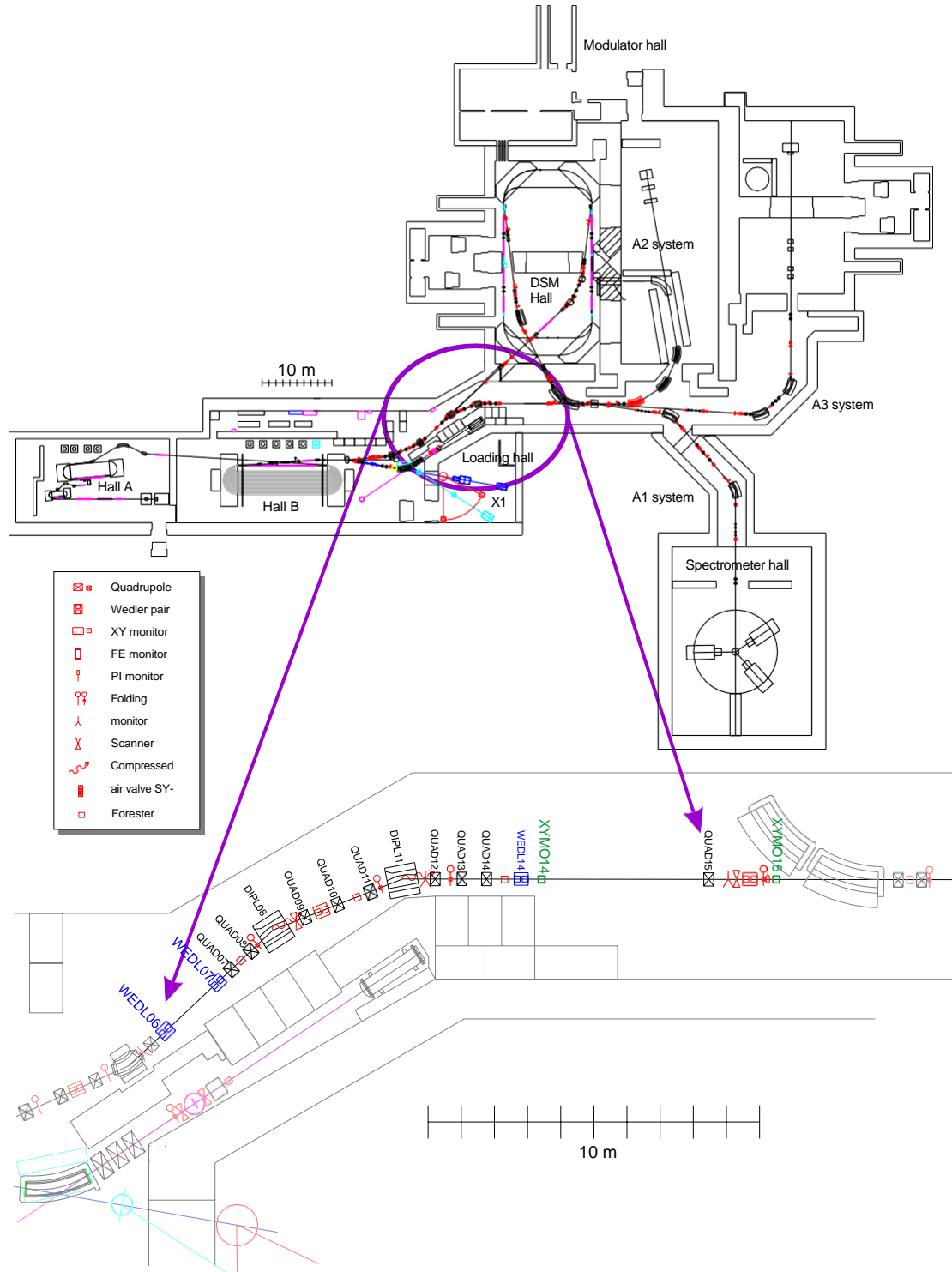


Figure 2.1: *Top:* Overview of the accelerator facility
Below: Second section of the transfer system (T2 system)

2. beam optical measurement

coordinates are represented as vector a :

$$a = \begin{pmatrix} x \text{ [mm]} \\ x' \text{ [mrad]} \\ z \text{ [mm]} \\ z' \text{ [mrad]} \\ s \text{ [mm]} \\ \frac{\Delta p}{p} \text{ [%]} \end{pmatrix} \quad (2.1)$$

Here, (x, x') is the horizontal and (z, z') is the vertical position and direction in relation to a particle that is on the nominal trajectory (nominal particle). s and $\frac{\Delta p}{p}$ are the longitudinal coordinate and the momentum deviation relative to the target particle.

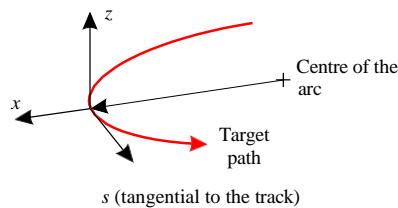


Figure 2.2.: Coordinate system moving with the target particle

This vector a is transformed as it passes through the various elements, whereby in the case of linear optics the transformation is described in each case by a matrix M_i (let the elements be numbered starting with 1):

$$\begin{aligned} a_n &= M_n \cdot a_{n-1} = M_n \cdot M_{n-1} \cdot a_{n-2} = \dots = M_n \cdot M_{n-1} \cdot \dots \cdot M_1 \cdot a_1 \\ &= M \cdot a_1 \end{aligned} \quad (2.2)$$

Dabei liefert die Matrix M die Transformation bezüglich des Gesamtsystems. In einem Strahlführungssystem, wie dem hier untersuchten, sind die x - und z -Bewegungen in guter Näherung entkoppelt, so dass die zugehörigen Phasenräume getrennt behandelt werden können. Die longitudinalen Parameter s und Δp sind hier nur der Vollständigkeit halber aufgeführt; sie sind mit den im Rahmen dieser Arbeit verwendeten Methoden nicht direkt erfassbar. Damit wird aus Gleichung 2.2

$$\begin{aligned} a_{nx} &= \begin{pmatrix} m_{11} & m_{12} \\ m_{21} & m_{22} \end{pmatrix} \cdot \begin{pmatrix} x_1 \\ x'_1 \end{pmatrix} = M_x \cdot a_{x1} \quad (2.2^t a) \\ a_{nz} &= \begin{pmatrix} m_{31} & m_{32} \\ m_{41} & m_{42} \end{pmatrix} \cdot \begin{pmatrix} z_1 \\ z'_1 \end{pmatrix} = M_z \cdot a_{z1} \quad (2.2^t b) \end{aligned}$$

2.1 Matrix formalism

In the following, the matrices for the beam guidance components are introduced. A detailed derivation can be found for example in [CAS84], [CAS86], [SLC72] or [Bro80].

2. beam optical measurement

2.1.1. Drift track

The simplest transformation is performed by a drift path of length l : The trajectory of the particles is not influenced.

$$M_x = M_z = \begin{pmatrix} 1 & l \\ 0 & 1 \end{pmatrix} \quad (2.3)$$

2.1.2. Dipole

The important parameters for setting up the mapping matrix of a dipole deflecting magnet with the central magnetic field B are the radius ρ

$$\rho = \frac{p}{eB} \quad (2.4)$$

for the target particle with momentum p and charge e . From this follows its deflection angle ϕ and the polar edge angles δ_1 and δ_2 (see figure 2.3). The shape of the boundary field determines the parameters

$$k_1 = \frac{Z + \infty B_z(u) - B_0}{gap - B_0^2} \quad (2.5)$$

$$k_2 = 4.4 \quad (2.6)$$

is defined. Here $B_z(u)$ is the course of the vertical field component along the normal to the leading or trailing edge, B_0 is the magnetic field inside the dipole and gap is the gap height. The parameter k_2 takes into account the shape of the boundary field. For the Rogowski profile of the magnetic poles in our case, a relatively far-reaching boundary field results (see figure 2.4), which is to be characterised with $k_2 = 4.4$ according to [Bro80]. These two parameters in turn serve as a correction of the entrance angle δ_i ([Bro80], [SLC72]):

$$\psi_i = \frac{gap}{\rho} \left\{ \frac{1 + \sin^2 \delta_i}{\cos \delta_i} \right\} \left\{ \frac{gap}{\rho} \tan \delta_i \right\} \quad (2.7)$$

Furthermore, it is possible to calculate a radial field gradient by specifying the field index.

$$n = - \frac{\rho}{B_0} \frac{\partial B_z}{\partial r} \Big|_{r=\rho} \quad (2.8)$$

to be account.

The transformation matrix M_{Dipole} of such a deflecting magnet results from the connection of these matrices in series:

$$MDipole = M_{Outlet} \cdot M_{Sector\ magnet} \cdot M_{Inlet} \quad (2.9)$$

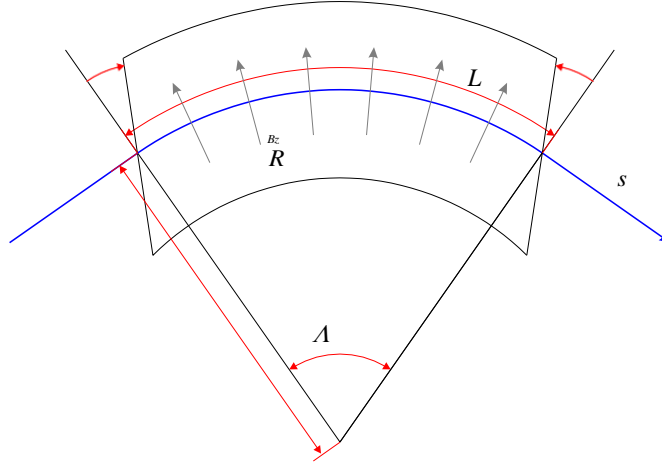


Figure 2.3: General deflecting magnet with entry and exit angle (sign convention according to [SLC72]), as well as a field gradient.

M_{Einlet} and $M_{Aoutlet}$ act like two infinitely thin lenses which focus the beam vertically for $\delta_i \psi_i > 0$. $M_{Sector magnet}$ is the matrix of a sector magnet without a boundary field, into which the beam enters and exits perpendicularly to the pole edges.

According to [SLC72] one obtains¹:

$$M_{xDipol} = \begin{pmatrix} 1 & 0 \\ \frac{\tan \delta_2}{\rho} & 1 \end{pmatrix} \begin{pmatrix} \cos(\sqrt{1-n}\phi) & -\frac{\rho}{1-n} \sin(\sqrt{1-n}\phi) \\ \frac{1}{\rho} \sin(\sqrt{1-n}\phi) & \cos(\sqrt{1-n}\phi) \end{pmatrix} \begin{pmatrix} 1 & 0 \\ \frac{\tan \delta_1}{\rho} & 1 \end{pmatrix} \quad (2.9^t (a))$$

$$M_{zDipole} = \begin{pmatrix} 1 & 0 \\ -\frac{\tan(\delta_2 - \psi)_2}{\rho} & 1 \end{pmatrix} \begin{pmatrix} \cos(\sqrt{n}\phi) & \frac{\rho}{n} \sin(\sqrt{n}\phi) \\ \frac{1}{\rho} \sin(\sqrt{n}\phi) & \cos(\sqrt{n}\phi) \end{pmatrix} \begin{pmatrix} 1 & 0 \\ -\frac{\tan(\delta_1 - \psi)_1}{\rho} & 1 \end{pmatrix} \quad (2.9^t (b))$$

The two identical deflection magnets of the T2 section originate from the beamline of the Institute's former 300 MeV linear accelerator and were adapted to higher beam energies by reducing the air gap height to 28 mm.

¹For the sake of clarity, the x and z coordinates are shown separately here.

2. beam optical measurement

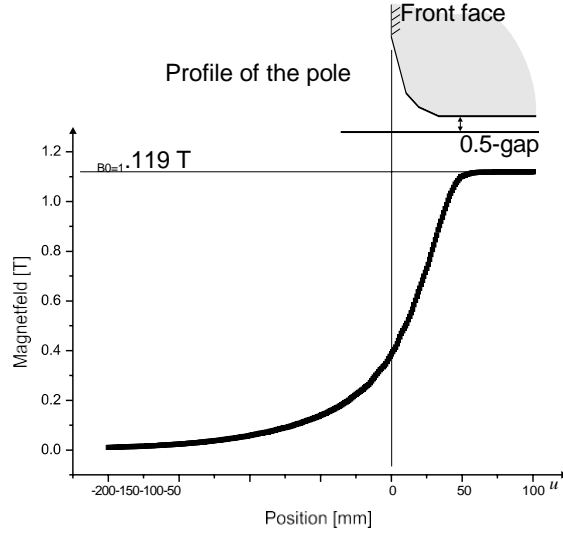


Figure 2.4: Field curve of DIPL11 simulated with FEMM: The effective field boundary coincides with the face area of the magnet.

Since no field measurements could be carried out due to time constraints, the boundary field was calculated using the two-dimensional simulation programme FEMM (see figure 2.4) and the relevant parameter $k_1 = 0.84$ was determined for the imaging properties. They have parallel leading and trailing edges and deflect the beam by 21.5° in each case. The effective radius of curvature is 2.45 m. Since the entry and exit angles are equal, $\delta_1 = \delta_2 = \phi/2$.

2.1.3. Quadrupole

According to [CAS84], for the horizontal and vertical mapping matrix of a quadrupole-magnet with the field gradient $g = \frac{\partial B}{\partial x}$ and the effective length l :

$$\begin{aligned}
 M_{x\text{Quadrupole}} &= \begin{pmatrix} \cos(\sqrt{k} \cdot l) & \sin(\sqrt{k} \cdot l)/\sqrt{k} \\ -\sin(\sqrt{k} \cdot l)/\sqrt{k} & \cos(\sqrt{k} \cdot l) \end{pmatrix} \\
 M_{z\text{Quadrupole}} &= \begin{pmatrix} \cosh(\sqrt{k} \cdot l) & \sinh(\sqrt{k} \cdot l)/\sqrt{k} \\ \sinh(\sqrt{k} \cdot l)/\sqrt{k} & \cosh(\sqrt{k} \cdot l) \end{pmatrix}
 \end{aligned} \tag{2.10}$$

Here $k = g \cdot \frac{e}{p}$. For positive k , the quadrupole is horizontally focussing and vertically defocussing.

2.2. Principle of measurement

The section T2 of the transfer system to be measured beam-optically (see Figure 2.1) was illuminated as sketched in Figure 2.5 with the aid of two wedlers (WEDL06 and WEDL07), the properties of which are described in detail in Annex A. The position and direction of the electron beam were determined using two RF position monitors at the exit (XYMO14 and XYMO15). Two RF position monitors at the exit (XYMO14 and XYMO15) were used to determine the location and direction of the electron beam. The details of the calibration of these monitors can be found in chapters 3 and 4.

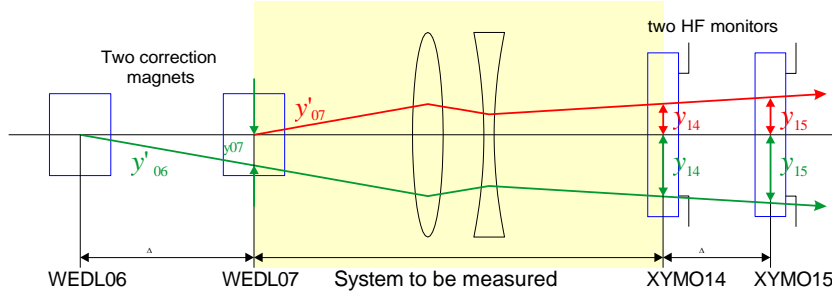


Figure 2.5.: Principle for measuring the T2 system

2.2.1. Procedure for determining the matrix elements

In order to determine the matrix elements m_{ij} of the transfer matrix M , four measurements must be carried out and evaluated according to the following equation:

$$\begin{pmatrix} x_{t14} \\ z_{t14} \\ z_{t14} \\ 1 \end{pmatrix} = \begin{pmatrix} m_{11} & m_{12} & 0 & 0 \\ m_{21} & m_{22} & 0 & 0 \\ 0 & 0 & m_{33} & m_{34} \\ 0 & 0 & m_{43} & m_{44} \end{pmatrix} \begin{pmatrix} x_{t07} \\ z_{t07} \\ z_{t07} \\ 1 \end{pmatrix} \quad (2.11)$$

Following [CAS84], in the following y is to be understood as representing both the x - and the z -component.

1. Measurement:

The first measurement was carried out with WEDL07 (variation of the beam direction y^{t_a}), whose position also defines the input of the T2 system. While the deposit behind the system could be measured directly with XYMO14 as y^a mm, the direction can be determined from the difference between the readings of XYMO15 and XYMO14 and their distance. This gives the equation

$$\begin{pmatrix} y^a \\ y_{14}^{t_d} \end{pmatrix} = M_y \begin{pmatrix} 0 \\ y_{07}^{t_a} \end{pmatrix} \quad (2.12)$$

with $y_{14}^{t_d} = \frac{y^a - y^a}{d_{14 \rightarrow 15}}$

2. Measurement:

In this measurement, the beam direction in *front* of the T2 system was changed with WEDL06 (y^{tb}). This caused a variation of the beam direction at the entrance of the system. location as well as the direction. The location was again measured in XYMO14 as y^b , the Direction y_{14}^{tb} was determined as above. One obtains with the distance $d_{06 \rightarrow 07}$ between WEDL06 and WEDL07 $y_{07}^b = y_{06}^{tb} - d_{06 \rightarrow 07}$ and $y_{07}^{tb} = y_{06}^{tb}$ the equation

$$\begin{pmatrix} y_{14}^b \\ y_{14}^{tb} \end{pmatrix} = M_y \begin{pmatrix} y_{07}^b \\ y_{07}^{tb} \end{pmatrix} \quad (2.13)$$

Calculation of the matrix elements:

To reduce the statistical error, each of the above measurements was carried out for many different y_{06}^{tb} and y_{07}^{tb} . This also made it possible to check the linearity and freedom from coupling of the optics.

The matrix elements should be determined from these two sets of measurements.

From equation 2.12 (1st measurement) follows:

$$m_{12} = \frac{y_{14}^a}{y_{07}^{ta}} \quad (2.12^t (a))$$

$$m_{22} = \frac{y_{14}^a}{y_{07}^{ta}} = \frac{y_{15}^a - y_{14}^a}{\frac{d_{14 \rightarrow 15}}{y_{07}^{ta}}} \quad (2.12^t (b))$$

With the help of Equation 2.13 and the matrix elements m_{12} and m_{22} the missing two matrix elements m_{11} and m_{21} were calculated (2nd measurement):

$$m_{11} = \frac{y_{14}^b}{y_{07}^b} = \frac{y_{14}^b}{y_{06}^{tb} - d_{06 \rightarrow 07}} - \frac{y_{06}^{tb}}{d_{06 \rightarrow 07}} - m_{12} \quad (2.13^t (a))$$

$$m_{21} = \frac{y_{14}^{tb}}{y_{07}^b} = \frac{y_{14}^{tb}}{y_{06}^{tb} - d_{06 \rightarrow 07}} - \frac{y_{06}^{tb}}{d_{06 \rightarrow 07}} - m_{22} \quad (2.13^t (b))$$

Both measurements were carried out for the horizontal as well as for the vertical.

2.3. Measuring routine

2.3.1. Input parameters before starting a measurement

Illumination with the help of wedlers

From the wedge calibrations described in Appendix A, the sensitivity of the differently constructed wedges was determined.

$$\frac{y_{0t}}{I}^6 = 0.952 \pm 0.015 \frac{\text{mrad}}{\text{A}}$$

$$\frac{y_{0t}}{I}^7 = 0.682 \pm 0.015 \frac{\text{mrad}}{\text{A}}$$

In order to reduce hysteresis effects, the diverters ran through a cycle (+4 A, -4 A, 0 A; each for about 200 ms) before setting the desired deflection angle, in the following referred to as „cycling”), in order to have as comparable a history as possible.

Parameters of the electron beam

The measurements were carried out with diagnostic pulses whose amplitude was set to a constant peak value of 50 μA for all measurements. The repetition frequency was 640 Hz, so that the influence of the mains hum could be minimised by 64 averages (more details on the diagnostic pulses in 3.3 and subsection 4.2.3).

Calibration of the xy monitors

The signals of the xy -monitor XYMO14 were directly calibrated with the mechanics described in chapter 4. For the second monitor XYMO15, which was not equipped with this system, the calibration had to be done with the help of the electron beam by also calibrating the wedler WEDL14 located close in front of XYMO14 (see figure 2.6). As can be seen in figure 2.1, the quadrupole QUAD15 is located between the two monitors, which was switched off but had to be accounted in the calibration due to its remanence field. The exact properties of the monitors are discussed in more detail in chapter 3 and [Her78] and the calibration in chapter 4.

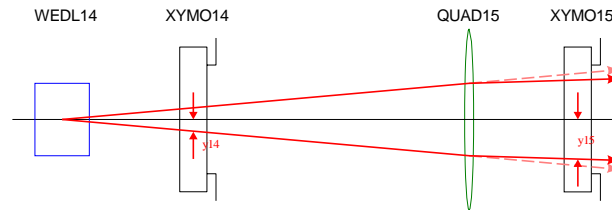


Figure 2.6: Calibration of XYMO15

Reference track

Before starting a measurement, the reference trajectory was defined. For this purpose, the beam was placed centrally in the quadrupoles and position monitors by a standard optimisation routine.

2.3.2. Input parameters before each measurement series

Adjusted jet trays

In order to determine the area to be illuminated, the beam was deflected from the nominal path so far that the achieved deposition y_{14} or y_{15} in the *xy monitors* was just under 2 millimetres in each case. The beam should not hit the beam pipe or other obstacles during the measurement, as a scattered beam would also generate a signal in the *xy monitor* that would be difficult to distinguish from a *real* signal.

Parameters of the measuring routine

With the software, it was possible to determine whether the wedge current should be linearly changed horizontally and vertically in each cycle or randomly adjusted. The advantage of random adjustment was that both hysteresis effects and a slow drift of the beam cancelled out over averaging (see figure 2.8). The majority of the measurements were therefore carried out using this method.

2.3.3. One measuring cycle

During each series of measurements, the measuring programme set the wedge current in a cycle and waited 250 milliseconds after the acknowledgement signal of the wedge control. Waiting times longer than 250 milliseconds did not cause any significant change in the measurement results. The routine then let the oscilloscope average 64 pulse signals from the *xy monitors*, transferred the averaged pulse signal to the computer and determined the integral from the beginning of the pulse to its zero crossing. The Wedler current and the pulse integral were saved together in a file which was later evaluated, as shown by an example in figure 2.8.

2.4. Optical settings

The ideal optical properties of the T2 system, symmetrically constructed from QUAD07 to QUAD13, are illustrated in Figure 2.7 (*above*). It is telecentric and achromatic. The effective drift distances in the horizontal and vertical planes are of the same order of magnitude (matrix elements m_{12} and m_{34} of the matrix M_{ideal}). The transverse sale imaging matrix M_{ideal} was determined with the interactive simulation programme BEAMOPTIK [*ShvoO*].

$$M_{ideal} = \begin{pmatrix} -0.991 & -7.726 & 0 & 0 \\ 0.005 & -0.967 & 0 & 0 \\ 0 & 0 & -0.961 & -5.420 \\ 0 & 0 & 0.007 & -1.001 \end{pmatrix}$$

This also determined the quadrupole strengths of the eight quadrupoles required for this setting. In order to determine the excitation strength of the quadrupoles, the

2. beam optical measurement

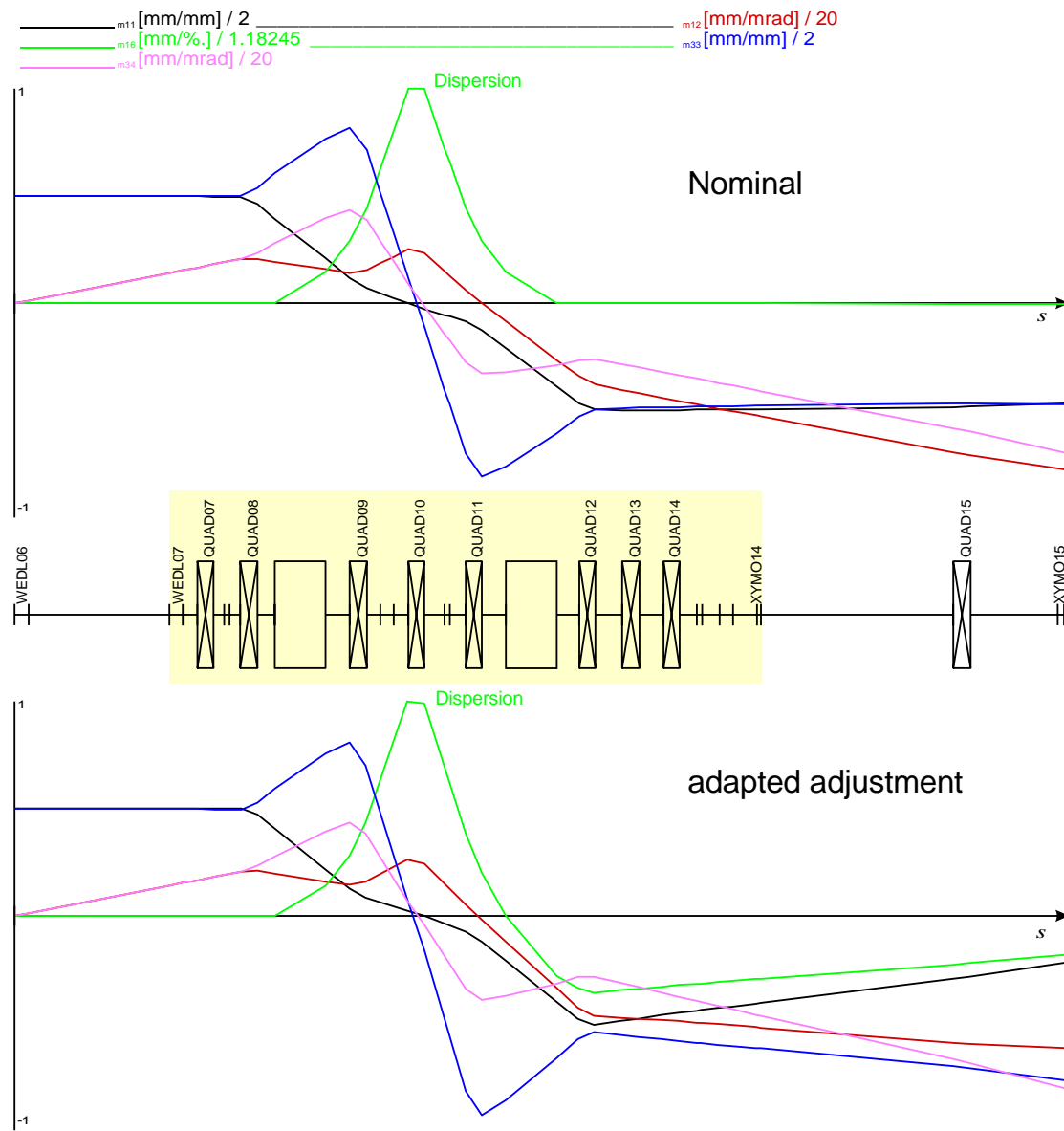


Figure 2.7.: The horizontal and vertical trajectories and additionally the dispersion along the T2 system are shown.

Top: Set setting

Below: later model adapted to measurement

Quadrupole strength first converted linearly into the required excitation current on the basis of the data sheet values without taking into account remanence and saturation effects.²

2.5. Evaluation

2.5.1. Setting up the matrix

From the raw data of the measurement routine described above, the relationship beam position y_i vs. deflection angle y_{it} was fitted by a straight line whose slope a the desired measurand (for example $a = y_{14}^{14}$ as shown in Figure 2.8 (a)). In This example further shows that the assumption of a linear mapping matrix is justified. Similarly, no systematic coupling between the horizontal and vertical planes is apparent, which is shown in Figure 2.8 (b). If a coupling were present, the magnitude of the vertical pulse intensity in this example would have to be grals depend on the horizontal deflection (i.e. $a^{07} x_{14z} = 0$). With the coefficients a determined in this way, the matrix elements could now be calculated according to equations 2.^{12t} (a) to 2.^{13t} (b). be calculated:

$$M = \begin{pmatrix} -1.182 \pm 0.53 & -8.423 \pm 0.34 & 0 & 0 \\ 0.042 \pm 0.06 & -0.607 \pm 0.05 & 0 & 0 \\ 0 & 0 & -1.449 \pm 0.26 & -5.583 \pm 0.17 \\ 0 & 0 & -0.077 \pm 0.05 & -0.977 \pm 0.04 \end{pmatrix}$$

The errors of the matrix elements are calculated from the measurement errors of the calibration as well as from the statistical uncertainty of the linear coefficients determined above.

2.5.2. Error analysis

A criterion for the quality of the measurement is the determinant of the matrix determined in this way. According to the Liouville theorem³, the determinant must be equal to one. This also applies to the two (2x2) submatrices separately, since there are no couplings between horizontal and vertical phase space.

The determinants of these submatrices are $det_x = 1.074 \pm 0.248$ for the horizontal matrix and $det_z = 0.986 \pm 0.080$ for the vertical plane, i.e. they are compatible with unity within their uncertainties.

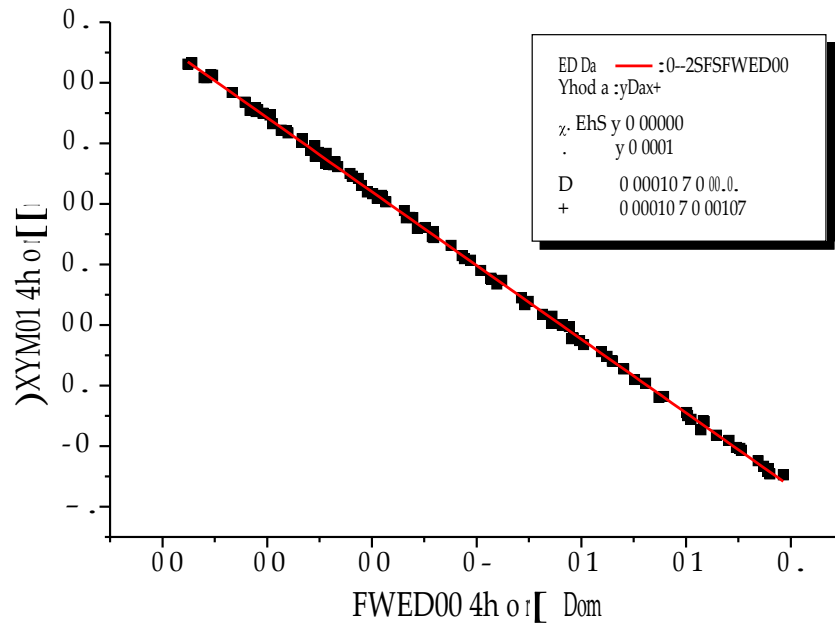
Um den Vergleich mit den Simulationsrechnungen zu vereinfachen, wurden die Kalibrationsfaktoren der Wedler und der xy-Monitore durch minimale und innerhalb der Fehler liegende Veränderung so angepasst, dass sich als Wert für die Determinanten in horizontaler und vertikaler Ebene jeweils Eins ergab. Dieses Vorgehen führte zu $det_x = 1.000 \pm 0.229$ and $det_z = 1.000 \pm 0.081$. The matrix elements themselves were given by

²The quadrupole model, as shown in figure B.1, was only developed later; for this reason the actually set quadrupole strengths sometimes deviate strongly from the nominal strength.

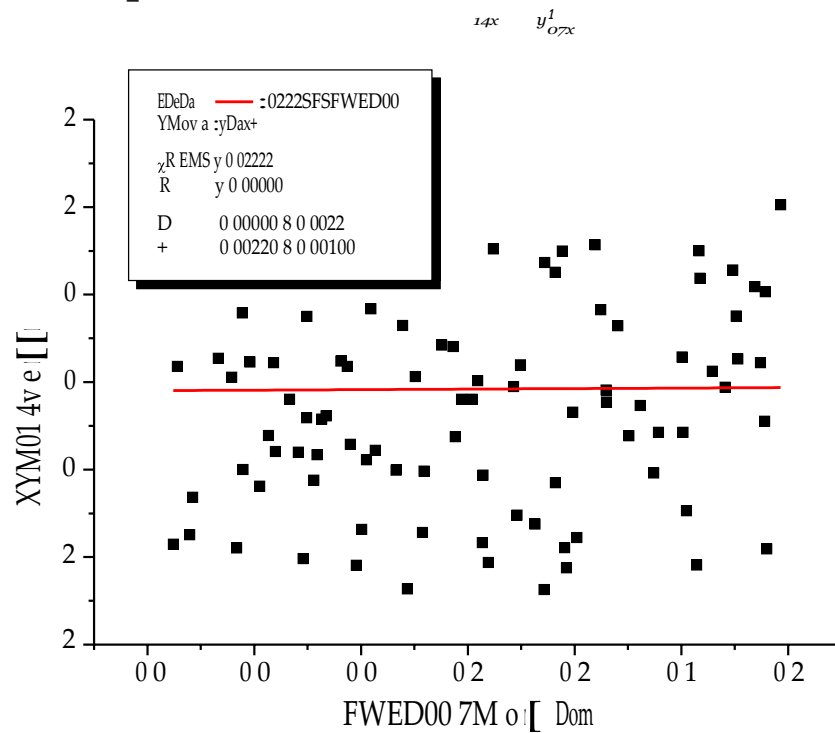
2. beam optical measurement

³The derivation can be found in relevant literature such as [Wil96].

2. beam optical measurement



(a) Determination of the measuring point a^{07x} (linearly adjusted)



(b) Check for coupling ($a^{07x} c:: o \Rightarrow$ negligible)

Figure 2.8.: Measured deposits in XYMO14 as a function of the horizontal angle and - rung by WEDL07 with straight line fit through the measured values. The result in (b) shows that there is no measurable influence of the horizontal movement on the vertical deposit.

this procedure is only slightly altered:

$$\begin{array}{ccc} -1.146 \pm 0.54 & -8.098 \pm 0.36 & 0 \\ \overline{M} & 0.042 \pm 0.07 & -0.578 \pm 0.04 \\ 0 & 0 & -1.455 \pm 0.26 & -5.614 \pm 0.17 \\ 0 & 0 & -0.078 \pm 0.05 & -0.989 \pm 0.04 \end{array}$$

2.6. Result: Adaptation of the model

To adapt the computer model of the T2 system (represented by the matrix BO) to the measured mapping matrix, an algorithm was developed that varies the eight quadrupoles and the field gradients of the deflecting magnets in such a way that, according to Gleit-

2.14 results in as good a match as possible between the measured and simulated matrix. As a result, the programme delivered a BEAMOPTIK-compatible output.

The following table shows the quadrupole strengths required for this setting.

The fit algorithm minimised the sum of squared deviations of measured (m_{ij}) and calculated (bo_{ij}) matrix elements:

$$d = \frac{1}{N} \sum_{i,j=1}^4 \left(\frac{bo_{ij} - m_{ij}}{\Delta m_{ij}} \right)^2 \rightarrow \min \quad (2.14)$$

In the absence of couplings, $N = 8$, since the coupling matrix elements are equal to zero.

The result of the fit process was the transfer matrix BO :

$$BO = \begin{array}{ccc} -1.153 & -8.112 & 0 \\ 0.041 & -0.580 & 0 \\ 0 & 0 & -1.461 & -5.628 \\ 0 & 0 & -0.079 & -0.990 \end{array}$$

Figure 2.7 below provides a more descriptive overview. Here the most important trajectories of the matrix BO adapted to the measurement are shown.

Quadrupole strengths

Table 2.1 lists the quadrupole strengths matching BO . The sometimes quite large deviations between s_{ideal} and s_{BO} are largely due to the non-linear excitation curve (see Figure B.1), which, however, was only determined after this measurement. Especially in the case of smaller excitation currents, the quadrupole strength is not well described by the data sheets and the assumption of a linear dependence, which can be seen particularly clearly in QUAD12. For QUAD07, QUAD13 and QUAD14, an estimated residual field was at least partially taken account in the determination of M_{ideal} .

2. beam optical measurement

Table 2.1: List of quadrupole strengths: The values under *Sideal* represent the matrix M_{ideal} , under *SBO* the values matching *BO* are listed.

Quadrupole	<i>sideal</i> [T]	<i>S Fit</i> [T]	Dev. [%]	Current [A]
QUAD07	.033	.015	n.a.	0.00
QUAD08	1.177	1.020	-13.4	7.46
QUAD09	3.254	3.402	4.6	20.64
QUAD10	4.028	4.173	3.6	30.16
QUAD11	3.254	3.031	-6.8	20.64
QUAD12	1.116	1.460	30.8	8.36
QUAD13	.040	.030	n.a.	0.00
QUAD14	.002	.054	n.a.	0.00

Field indices of the deflection dipoles

The field indices in Table 2.2, which were determined by the Vital algorithm, may have resulted from manufacturing tolerances during the conversion. From the maximum field index found, n_{max} , the change of the magnetic field over width Δr of the pole shoe is extrapolated with equation 2.8, assuming a constant gradient:

$$\frac{\partial B}{\partial r} = \frac{\Delta B}{\Delta r} = n_{max} \frac{-B_0}{\rho} \quad (2.15)$$

$$\Rightarrow \Delta B = n_{max} \frac{B_0}{\rho} \Delta r \quad (2.16)$$

With the assumption $\frac{\Delta B}{B_0} = \frac{\Delta gap}{gap}$ it follows for the change of the air gap height

$$\Delta gap = \frac{\Delta B}{B_0} gap = \left\{ n_{max} \frac{-\Delta r}{\rho} \right\} gap \quad (2.17)$$

If one now sets the known values for $B_0 = 1.119$ T, $\rho = 2.45$ m, $n_{max} = 0.04$, $\Delta r \sim 0.3$ m, it can be seen that an error in the air gap height $\Delta gap 0.2$ mm causes a field index of this magnitude.

Table 2.2: List of the fitted field indices

Dipole	<i>nideal</i>	<i>nBO</i>
DIPL08	0.000	-0.030
DIPL11	0.000	-0.039

Part III.

Radiation diagnostics

3. HF position monitors

3.1. Basics of HF position monitors

The measurement of the beam position at MAMI is carried out, among other things, with the aid of HF monitors. They are installed at many points within the microtrons and in the beam feeds and allow a disturbance-free measurement of the beam positions both during the run-in with diagnostic pulses and during the experimental operation with c.w. beam.

The derivation of the theory of RF monitors was largely covered in a lecture by H. Herminghaus in the summer semester of 1978 [Her78] and can be found in Appendix C for the sake of completeness.

Short introduction:

The RF position monitors are constructed as *TM resonators*₁₁₀[Kla67], whose resonance frequencies are tuned to the bunch repetition frequency $\nu_0 = 2.44953$ GHz of the accelerator. The schematic of the monitor and the course of the field component $E_z(x, y)$, which is important for position measurement, are shown in Figure 3.1. If the beam is on the axis, no oscillation of this mode is excited. When the beam is deposited, the individual bunches of the beam excite a forced oscillation whose amplitude increases almost linearly with increasing deposition for highly relativistic particles.

From an electrical point of view, the resonator represents a local resistance (shunt impedance $r_{S_{110}}$), through which the beam current i flows. The following applies to the power stored in the resonator ($k = 2\pi/\lambda$ is the wave number of the excited frequency):

$$P_{Cav} = i^2 \cdot r_{S_{110}} = i^2 \cdot r_m \cdot (k \cdot x)^2 \quad (3.1)$$

with the parameter $r_m = 0.845$ M Ω , which depends only on the geometry of the resonator, the frequency and the material, and which was determined with the programme URMEL in a simulation [Eut98]. For the power coupled out with the aid of small antennas, the following applies:

$$P_{HF} = i^2 \cdot r_{S_{110}} \cdot \frac{\kappa}{(\kappa + 1)^2} \cdot \frac{1}{1 + \frac{Q_0}{\kappa + 1} \cdot \frac{\nu_0}{\nu_{Res.}}} \quad (3.2)$$

Here, the coupling $\kappa = 1.99$, the unloaded $Q_0 = 12610$, the resonance frequency $\nu_{Res.} = 2.44964$ GHz and the frequency $\nu_0 = 2.44953$ GHz used later in the mixer as a reference (local oscillator) are introduced. The numerical values of κ , Q_0 and $\nu_{Res.}$ refer to the resonator for the horizontal display of the XYMO14 to be calibrated.

3.2. Structure of the xy -monitor system

3.2.1. The xy monitor

The xy monitor consists of two aluminium cavity resonators arranged one behind the other, which have a common centre section. The length of this centre section is 30 mm, which is large enough to achieve sufficient decoupling between the x and y resonators in the order of -50 dB. The diameter of the resonators is 148 mm, the diameter of the radiating hole is 20 mm, the length 55.6 mm. This allows a TM_{110} mode to be excited at a frequency of $\nu_0 = 2.44953$ GHz.

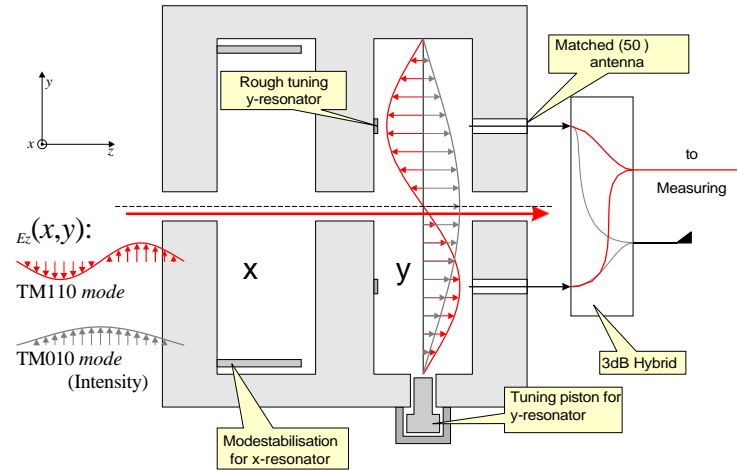


Figure 3.1.: Schematic structure of an xy monitor (Schumann type)

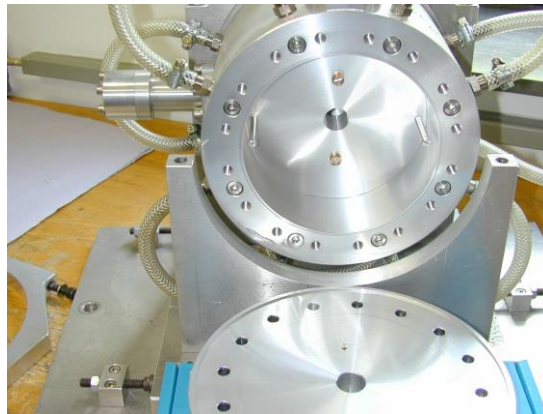


Figure 3.2.: An open „high-Q“ position monitor: You can see the two modest bilisators on the left and right edges of the resonator, through which here the horizontal TM_{110} mode is suppressed. (Photo Schumann)

The antenna pairs are embedded in the outer flanges (Figure 3.2).

3. HF position

capacitively couple out part of the field excited by the beam bunches. For coarse tuning of the resonance frequency, each resonator has two capacitance cylinders whose height of about 4 mm influences the resonance frequency. After the resonator has been roughly tuned and assembled, the tuning piston (left in Figure 3.2) can be used for fine tuning. The cancellation of the de-

The TM_{110} mode is controlled by means of two long cylindrical rods which raise the resonant frequency of the unwanted TM_{110} mode by about 80 MHz compared to the bunch frequency. With an unloaded quality factor of the order of 10^4 , the-

This means that its signal is phase-shifted by 90° in relation to the TM_{110} mode (under-pressure in the DBM) and only very small amplitudes can be expected.

3.2.2. The measurement electronics

The principle circuit diagram is shown in Figure 3.3. The signals coupled out of phase by the two antennas by 180° are subtracted in a 3dB hybrid and after passing through a low-pass filter, which is possibly intended to suppress higher frequency components, amplified in an RF amplifier. Subsequently The signal is mixed with the RF reference in a „Double Balanced Mixer“ (DBM for short), which, in the case of the same phase and the same frequency, produces a maximum output spanning. The components with the sum frequency are filtered out in an integrated low-pass filter so that only a voltage U_{DBM} modulated with the difference frequency $\Delta\omega = \omega_{HF} - \omega_{LO}$ is present at the-output of the DBM (let A be an arbitrary amplitude factor):

$$U_{DBM} = A \cdot \cos(\Delta\omega \cdot t + \Delta\phi) \quad (3.3)$$

The phase difference $\Delta\phi$ can be influenced by means of the phase shifter consisting of a circulator and a short-circuit shifter.

With the help of LF amplifiers, the signal is amplified even further (the diagnostic pulse branch is also electrically isolated) and fed to the multiplexer. By controlling the multiplexer accordingly (figure 5.1), the desired signal can be routed to the control room.

3.2.3. Calibration of the measuring electronics

In order to improve the sensitivity and the linearity of the sound signals connected to the HF monitor

To check performance, the 3dB hybrid of the horizontal resonator was placed behind the signal from a measuring transmitter. The reference was also supplied by this measuring transmitter, as otherwise phase stability (beat due to detuning of two transmitters) could not be guaranteed. Figure 3.4 shows a schematic of the measurement setup. The result shown in figure 3.5 (a) shows, as expected according to figure 3.3, a almost linear dependence between the output voltage U_x and the square root of the input power $\sqrt{P_{HF}}$. For the horizontal signal processing electronics, the following was determined the input power of about $0.7 \mu W$ over four orders of magnitude with the Step-Attenuator was steamed. In a second run, at constant power, the

3.2 Structure of the xy monitor

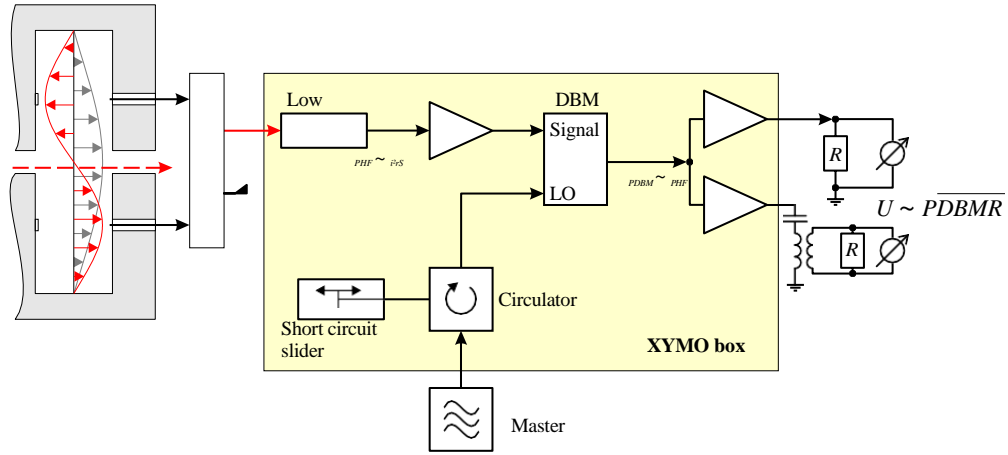


Figure 3.3.: Scheme of signal processing of an HF monitor (concept H. Mussel)

The phase of the signal is tuned with respect to the reference phase. Here, too, the measuring electronics work as expected according to equation 3.3 (figure 3.5 (b)).

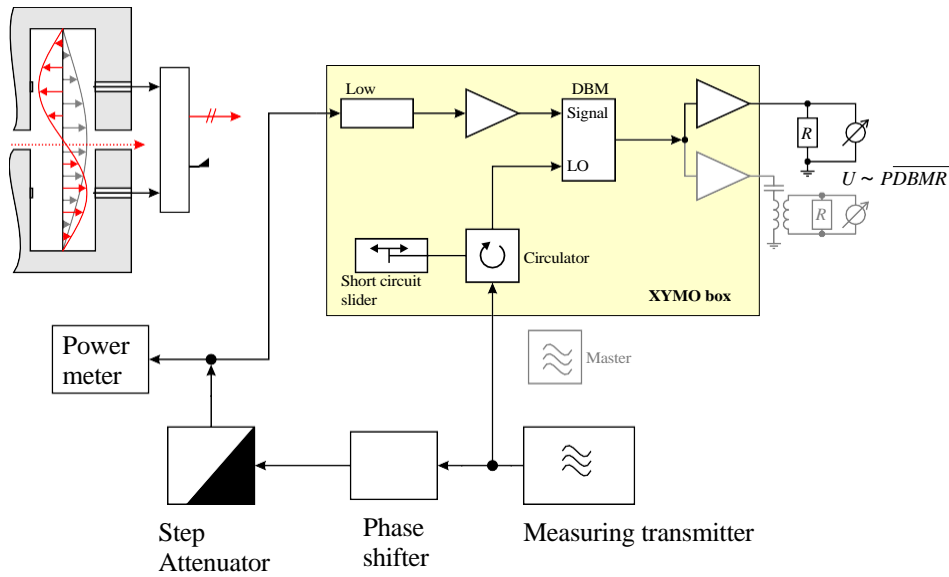
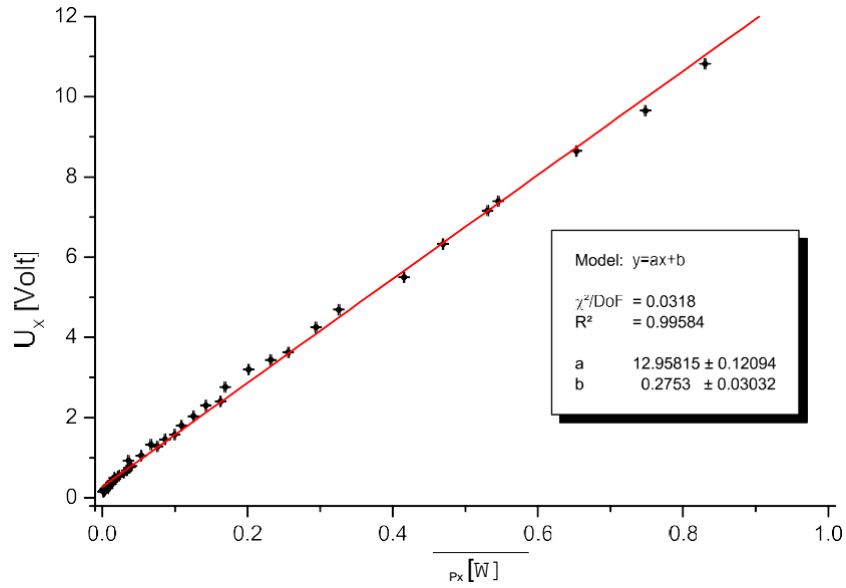


Figure 3.4: Arrangement for calibrating the measuring electronics (schematic)

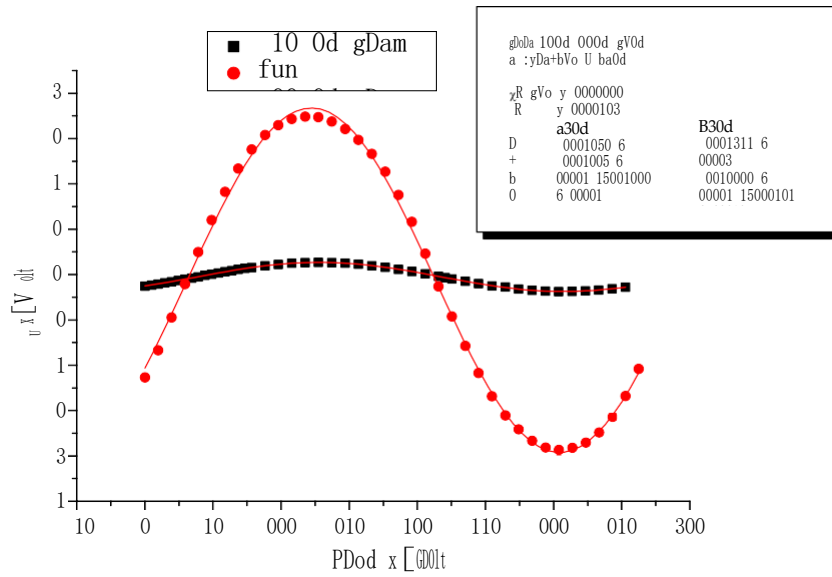
As calibration one obtains from this measurement

$$U_x = 13.0 - \sqrt{P_{HF}} [\mu W] + 0.1 \quad (3.4)$$

3. HF position



(a) Output voltage of the measuring electronics as a function of the square root of the HF power at the input of the low-pass filter (see figure 3.4)



(b) Output voltage of the measuring electronics as a function of the reference phase at the LO input of the DBM (with adjusted sine curve)

Figure 3.5: Calibration of the measuring electronics

In summary, the expected signal can now be calculated with equation 3.2. For an unloaded quantity $Q_0 = 12610$, coupling $\kappa = 1.99$, the resonator as well as the reference frequency of 2.44953 GHz, an expected output power of $P_x = 0.493 \text{ nW}/(\text{mm}\cdot\mu\text{A})$ is calculated. According to equation 3.4, this power should generate a signal voltage of $U_x = 0.409 \pm 0.09 \text{ V}/(\text{mm}\cdot\mu\text{A})$. The power $P_{\perp x}$ of the undesired $TM_{\perp 110}$ mode should, with a detuning of 80 MHz and the same rate, only be 0.027 nW. In addition, the phase of this non-resonantly excited mode is practically shifted by 90° , so that no measurable contribution is made by the mixing in the DBM. is to be expected.

3.3. Measurements with beam

In order to examine the sensitivity of this *xy monitor* in beam mode, an oscilloscope was used to digitise the voltage signals of the measuring electronics. As can be seen in figure 3.6, in addition to the DC voltage signal, an AC voltage component with a fundamental frequency of 50 Hz is also obtained, which is derived from the un-
The signal was therefore always averaged over a mains period of 20 ms. For the evaluation, the signal was therefore always averaged over a network period of 20 ms.

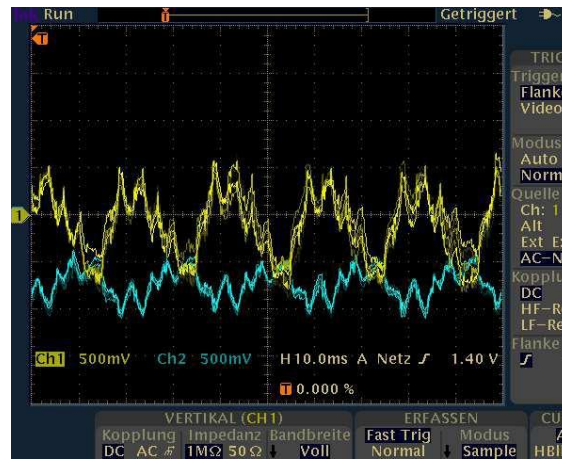


Figure 3.6.: Signal of the horizontal (yellow) and vertical (blue) beam deposition in the XYMO14 as a function of time for a c.w. beam of 10 μA

Local sensitivity

To determine the spatial sensitivity, the RF position monitor XYMO14 was shifted by about 1.5 mm in both directions from its nominal position using the calibration mechanics described in chapter 4. From the fit shown in Figure 3.7, a signal voltage $U_x = 2.16 \text{ V/mm}$ can be read (this corresponds to $U_x = 0.599 \text{ V}/(\text{mm}\cdot\mu\text{A})$). -

This value is 46 % greater than the theoretically predicted value. This difference can be explained by deviations in the resonator parameters and tolerances in the microwave

3. HF position

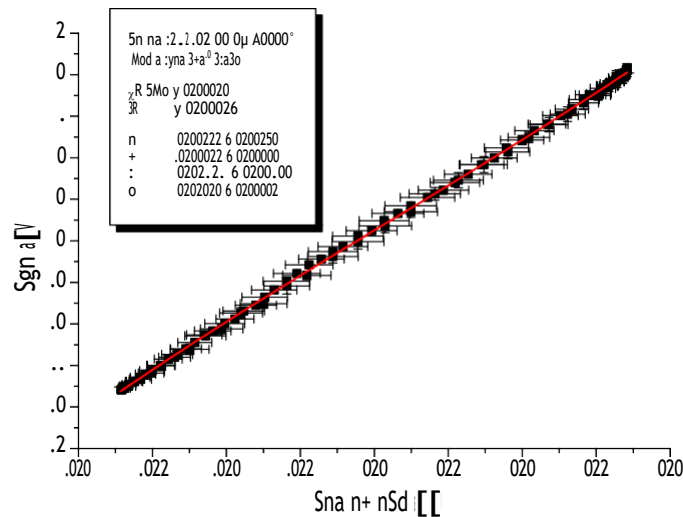


Figure 3.7.: Calibration of the deposition signals at a beam current of 3.6 μA at 855.15 MeV

components can be explained. Using the calibration from Figure 3.7 would then give the measured shunt impedance $r_{mt} = 1.238 \text{ M}\Omega$ for the horizontal Resonator.

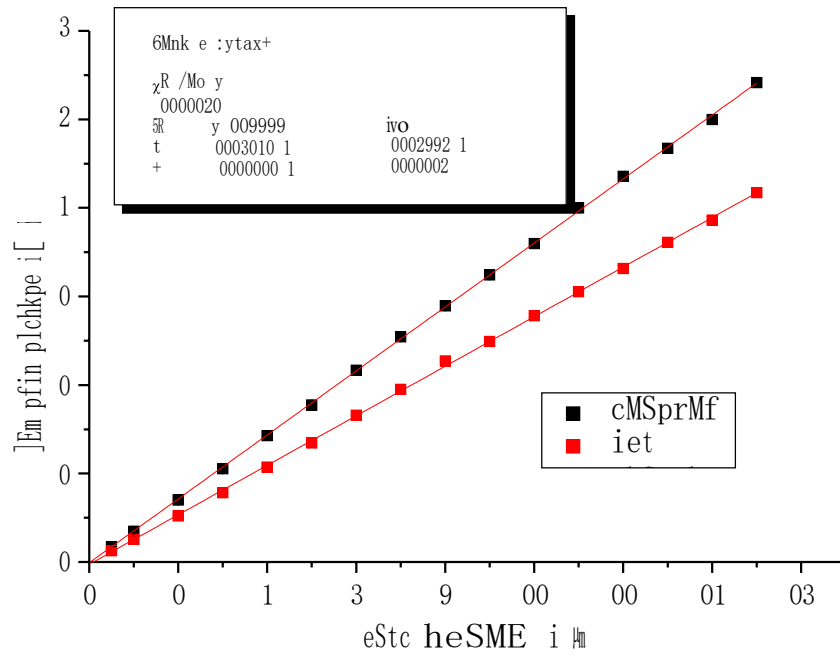
Beam current sensitivity

Measurements of the same type were carried out between some 0.5 μA and 15 μA and between 10 μA and 100 μA beam current. In the 2.45 GHz branch, a 6 dB attenuator was used at the output of the 3dB hybrid for the first set, and a 20 dB attenuator for the second set, in order to keep the signal in the 5 volt range. Nevertheless, for beam currents above 40 μA , the horizontal signal and above 60 μA also the vertical signal was cut off for large deposits, so that these ranges were not account in the evaluation.

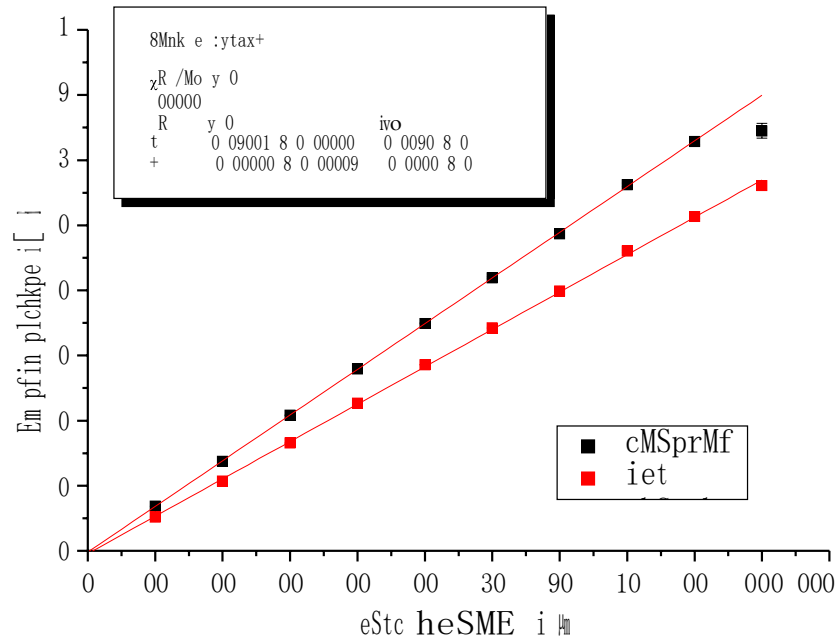
Figure 3.8 shows the result of all these measurements. The sensitivity of the monitor is indeed proportional to the beam current i , as predicted by theory.

Table 3.1: Beam current sensitivity XYMO14

D'ampfer	hori [mV/(mm- μA)]	vert [mV/(mm- μA)]
0 dB	$599.0 \pm 1 \%$	$446.5 \pm 1 \%$
6 dB	$361.0 \pm 1 \%$	$279.9 \pm 1 \%$
20 dB	$70.2 \pm 1 \%$	$57.4 \pm 1 \%$



(a) 6dB dampers between 0.5 and 15 μ A



(b) 20dB dampers between 10 and 100 μ A

Figure 3.8.: The sensitivity of XYMO14 as a function of the beam current can be regarded as linear.

3. HF position

Diagnostic pulses

The monitor also behaves as expected in beam mode with diagnostic pulses (see Figure 3.11). The diagnostic pulses are 12 ns long, have a typical amplitude of 100 μ A and a repetition rate of 10 kHz. Compared to the c.w. beam, they have the advantage that a clear signal is still generated in the RF monitors at a very low average current, the loss of which in the beamline does not lead to damage. This type of beam operation is therefore very suitable for adjusting the machine and was also used for beam-optical measurement.

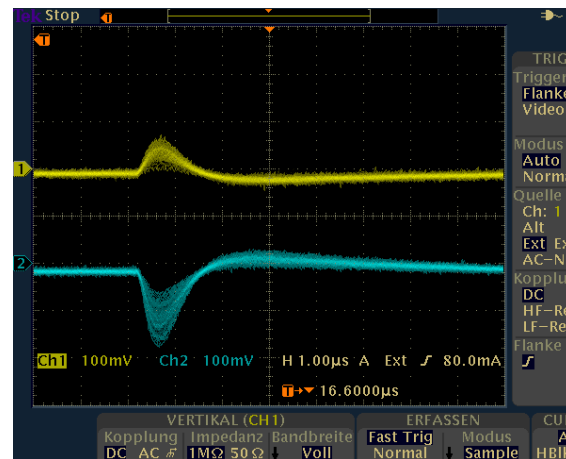


Figure 3.9.: Signal of the horizontal (yellow) and vertical (blue) beam deposition in the XYMO14 in diagnostic pulse mode

The output signal of the DBM is first integrated analogue (τ 3 ns) to suppress interference signals. The overshoot with opposite polarity is caused by the galvanic isolation; the signal must have the value zero on average. have.

Instead of the comparatively difficult determination of the pulse amplitude, the area from its beginning to its zero crossing is determined numerically as a measure of the height of the signal (figure 3.10). For this purpose, the signal is digitised with the aid of a digital oscilloscope and transferred to the computer.

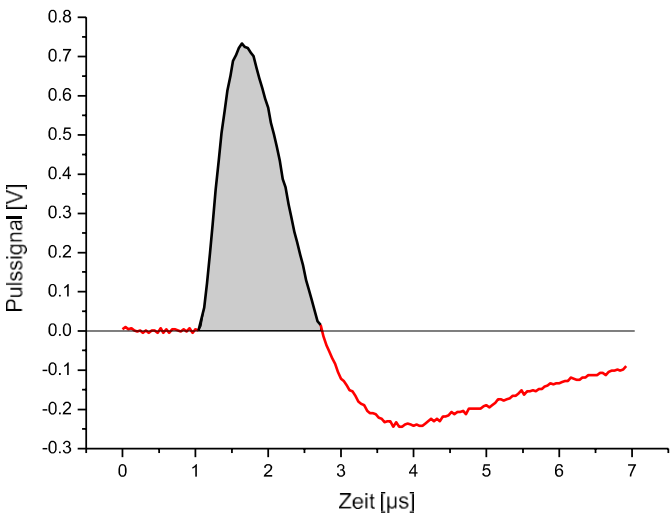


Figure 3.10.: Numerical pulse integration: The range from the beginning to the first zero crossing (grey area) is summed.

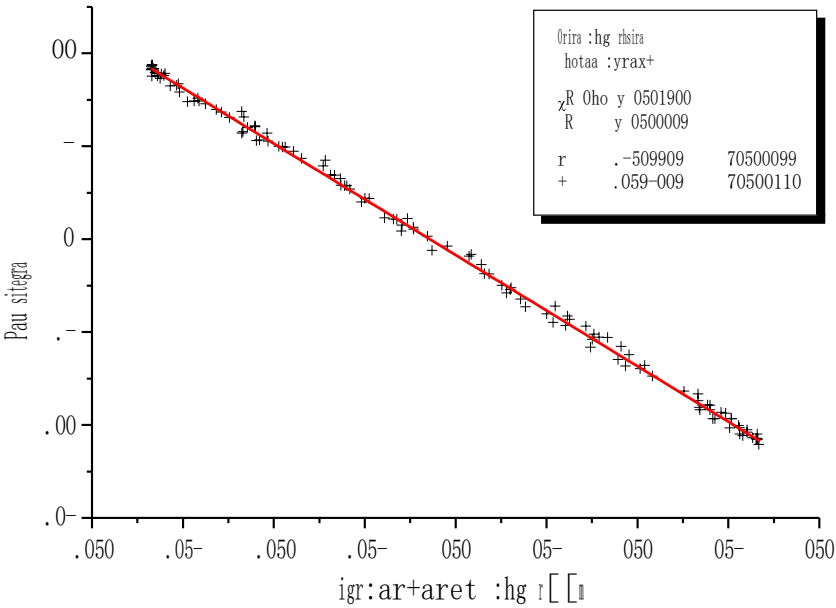


Figure 3.11.: Calibration of the deposition signals in diagnostic pulse mode at 855.15 MeV

3. HF position

3.4. Non-linearity of the sensitivity of the xy monitor

Using the lifting mechanism, numerous sensitivity measurements were carried out during various beam tests, in which different beam energies were also set. Some measurements showed slight s-shaped bends of the sensitivity curves for horizontal beam deposition (as shown in fig. 3.12 (a)), which were clearly outside the statistical error and could not be caused by a non-linearity of the position calibration.

In order to obtain further information about the non-linear effect, the sensitivity curves were recorded at different phases of the reference wave. As can be seen in figure 3.12 (b), the non-linearity increased and reached a peak.

maximum when the reference phase is rotated by $\Delta\phi_{ref}^{90^\circ}$. Similar effects

As expected, the same information was also found in the branch for the y -file. However, they are not discussed further here, as they do not contain any significantly different information.

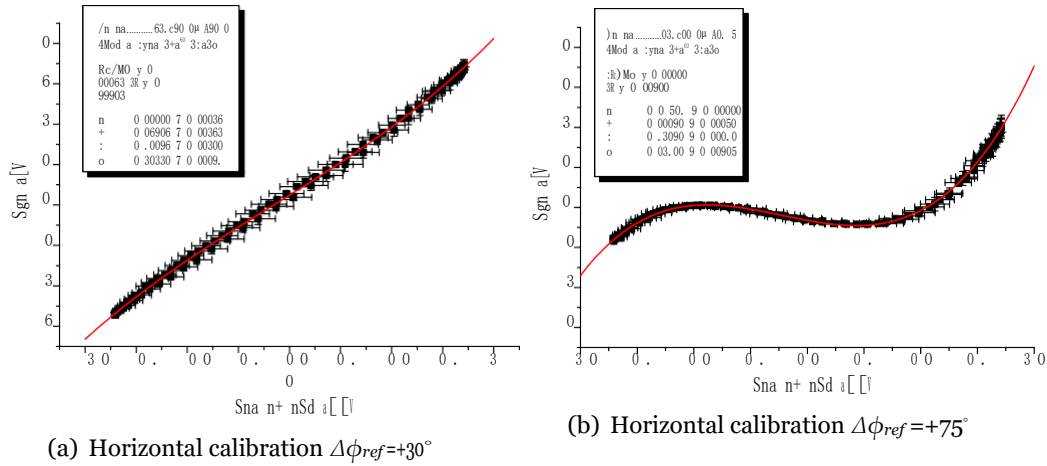


Figure 3.12.: Examples of calibration of the deposition signals at a beam current of $3.6 \mu A$ as in figure 3.7

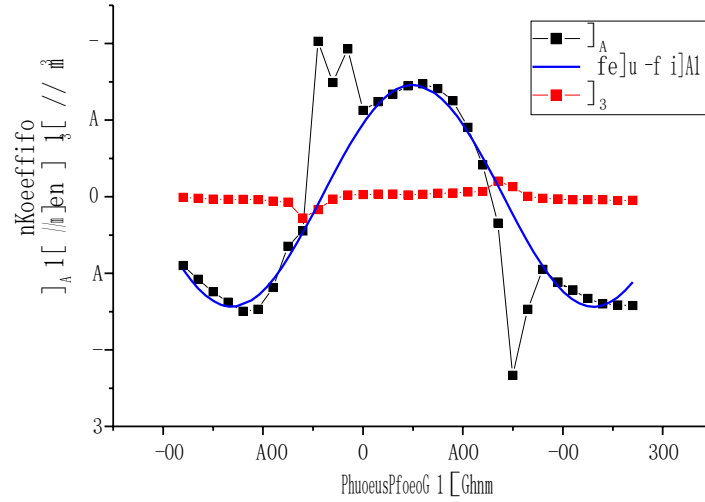
The initially obvious assumption that this was an admixture of the TM_{310} mode, which according to [Her78] has a cubic excitation characteristic and, like the TM_{110} mode, is amplified by subtraction of the two antenna signals, was not confirmed. Measurements with a network analyser showed that this oscillation mode, which is resonant at 4.1 GHz, is a loaded oscillation mode.

$Q_L = 4130$ and can thus only provide a contribution of the order of 10^{-5} at 2.45 GHz compared to the resonant TM amplitude.₁₁₀

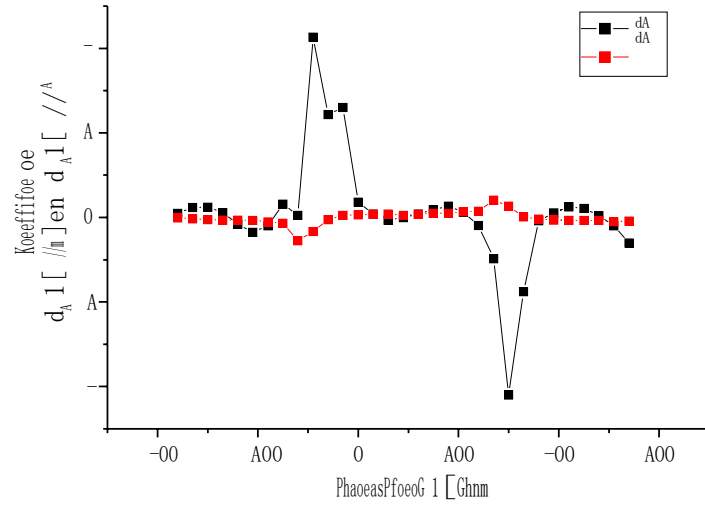
For further investigations, the measured sensitivity curves for each value of the adjusted reference phase were analysed with regard to their linear and cubic components. In figure 3.13 (a) the corresponding coefficients are plotted as a function of the phase of the reference wave. As can be seen, for certain values of ϕ_{ref} the curve for the linear component deviates strongly from the sinusoidal curve that would result in the case of a pure TM_{110} mode. (By entering the signal from a measuring

3.4. Non-linearity of the sensitivity of the xy monitor

The measurement electronics have been checked beforehand to ensure that they actually deliver such a sinusoidal curve, as shown in figure 3.5 (b). The cubic component delivers quite large contributions with different signs at a distance of 180° over a phase width of only about 30° ; in the areas in between, the contribution is almost identical. Zero.



(a) Sine curve adapted for A_1



(b) Sine curve subtracted for A'_1

Figure 3.13.: Course of the linear and cubic fractions ($\sim x$ and $\sim x^3$)

Assuming that the TM_{110} mode is excited in ideal form in the resonator, the corresponding sinusoidal curve was subtracted in the next step. The curve to be subtracted was determined by not account the strongly deviating points in the curve fitting (blue solid curve in Figure 3.13 (a)).

3. HF position

The result shown in figure 3.13 (b) shows that the remaining linear component has particularly high peaks in the phase range in which the cubic contribution is also different from zero. Outside of this range, the amplitude is much smaller and slightly ~~wade~~

This behaviour gives rise to the question of whether the observed non-linearity is a matter of harmonics which can be excited with a large amplitude due to the very short bunch length of the electron packets and are rectified in the DBM despite the measures taken to suppress them. The low-pass filter installed behind the hybrid is only effective from 2.7 GHz (3dB point) to around 8 GHz and selectively loses its effect more and more at higher frequencies. The extent to which the RF amplifier is permeable to very high frequencies and whether, for example, cross-couplings from the local oscillator to the signal input of the DBM allow rectification is a matter of debate.

Unfortunately, due to the limited time available, it was not possible to investigate this issue within the scope of this work.

4. Calibration of an HF position monitor

To determine the imaging properties of the T2 system, two calibrated position monitors are required, which are as far apart as possible.

XYMO14 and XYMO15 are particularly suitable for this purpose (see figure 2.1). However, these monitors have not yet been calibrated or have only been calibrated very roughly. In preliminary considerations, two possibilities of calibration were compared:

- 1. Calibration by changing the beam position:** One possibility of calibration is to change the beam position defined by a wedler. Apart from the problem of calibrating this wedler, only small beam streams can be set, since beam losses in the subsequent system are difficult to avoid.
- 2. Calibration by changing the position of the monitor:** Another method is to move the monitor to be calibrated precisely, not the beam, and thus calibrate the signals.

In the context of this work, the second method was implemented, as it promised greater accuracy and can be used at any beam current strength. The mechanics with which XYMO14 was moved during beam operation are now described here. The installation of the same mechanism for XYMO15 had to be dispensed with for the time being because of the relatively large effort involved. Instead, this monitor was calibrated using the calibration of XYMO14 by defined movement of the beam in approximate diagnostic pulse mode.

4.1. The lifting mechanism

A lifting mechanism for the XYMO14 HF position monitor was designed to meet the following requirements:

- The stroke should be greater than the beam position changes in normal beam operation. The goal was a displacement of about two millimetres in both directions.
- The velocity had to be large enough so that drifting of the beam position during calibration could not lead to large errors. However, it should be small enough to be able to average over at least one network period.
- The system should be used in the MAMI transfer system as far as possible, so that the monitor can be used at any time independently of the beamline used. A suitable position is XYMO14, which is located behind the T2 system to be measured beam-optically in chapter 2 (see figure 2.1).

4. calibration of an HF position

4.1.1. Principle of the lifting mechanism

The lifting mechanism was integrated into the existing adjustment frame (Figure 4.1 (a)). The right-hand threaded bolt used for height adjustment was replaced by a lifting mechanism with a swash plate¹ as sketched in Figure 4.1 (b). In order to obtain a defined axis of rotation and to reduce the moment of resistance against the bending of the two left-hand threaded bolts, these bolts were tapered in the middle area by turning them from 12 mm to 6 mm.

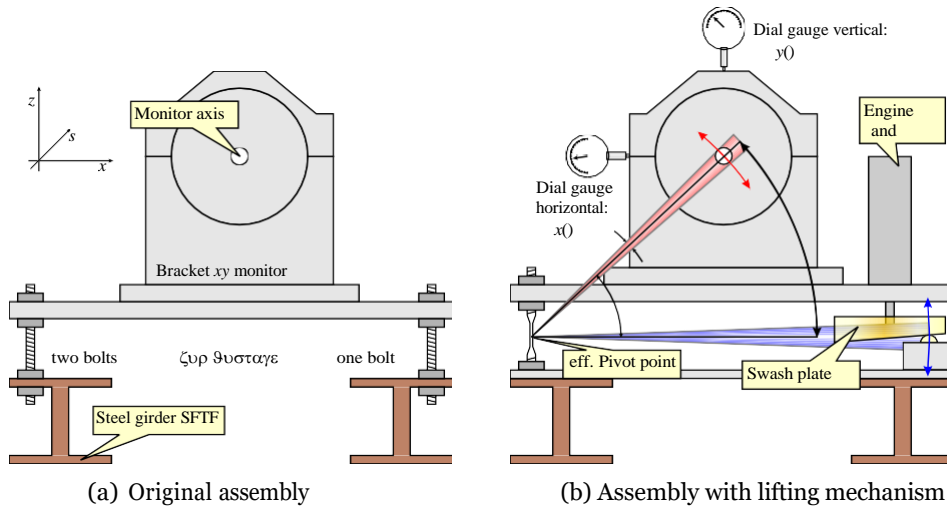


Figure 4.1.: Schematic of the XYMO14 frame before and after installation of the lifting mechanism

The movement on the beam axis of the monitor, which follows from the rotation of the swash plate, is indicated by the red arrow.

Swash plate

Figure 4.2 illustrates the principle of the swash plate. The disc has been linearly inclined in the x-direction (lower illustration). Its inclination is given by the angle ε :

$$\varepsilon = \arctan \left(\frac{\Delta h_{\text{disk}}}{2r_{\text{Disc}}} \right) \quad (4.1)$$

$$h(x, y) = h_0 + \tan \varepsilon \cdot x \quad (4.2)$$

The point of contact is defined by the angle θ to the x-axis and its distance r to the disc axis. Furthermore, o. b. d. A. $h_0 = 0$. With a transition to polar coordinates, one obtains the height variation $\delta h(r, \theta)$:

$$h(r, \theta) = r \tan \varepsilon \cdot \cos \theta = \Delta h \cos \theta \quad (4.3)$$

¹W. Klag: *private communications* 2003

4.1 The lifting

The ball bearing runs on the path marked as a thick black curve, while the swash plate rotates away under the bearing. With the parameters $2r_{disk} = 110$ mm and $\Delta h_{disk} = 8$ mm, $\varepsilon = 4.16^\circ$. With $2r_o = 100$ mm, $\varepsilon = 4.16^\circ$. the value of the maximum achievable stroke $\Delta h_o = r_o \tan \varepsilon = 3.64$ mm.

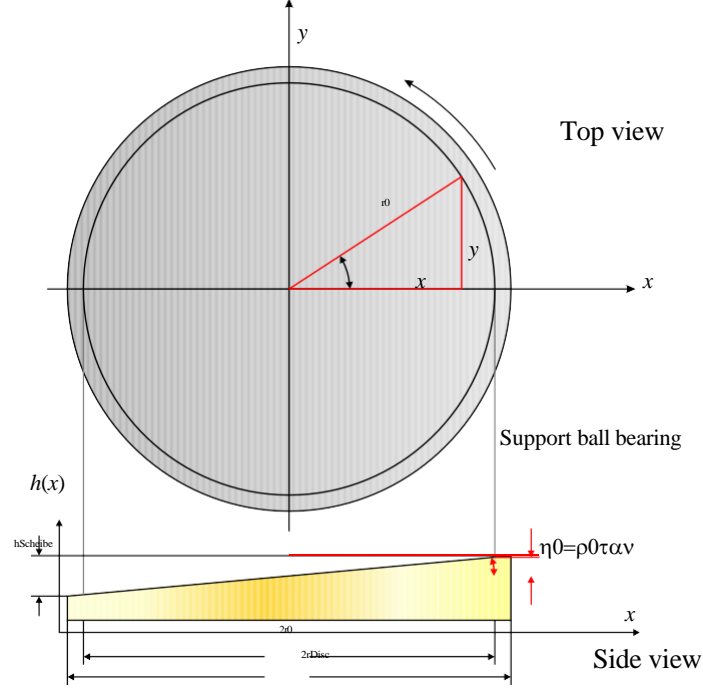


Figure 4.2.: Swash plate (principle)

Movement of the resonator

As indicated in Figure 4.1 (b) and Figure 4.3, the vertical motion caused by the swash plate is converted into a superposition of horizontal and vertical motion.

The position of the resonator axis is transferred to the axis in polar coordinates, since a rotation axis has been defined by the extension of the threaded bolts. The position of the monitor axis is in polar coordinates:

$$r_{Cav} = \sqrt{x_{oCav}^2 + y_{oCav}^2} \quad (4.4)$$

$$\varphi_o = \arctan \frac{y_{oCav}}{x_{oCav}} \quad (4.5)$$

The vertical movement \ddot{z} expresses itself in a rotation of the structure by the angle $\delta\varphi(\theta)$:

$$\delta\varphi(\theta) = \arctan \left\{ \frac{h(r_o, \theta)}{d_o} \right\} = \arctan \left\{ \frac{\Delta h_o - \cos \theta}{d_o} \right\} \quad (4.6)$$

4. calibration of an HF position

The position of the resonator axis as a function of the swash plate position θ is described by the angle $\varphi_0 + \delta\varphi(\theta)$:

$$x_{Cav}(\theta) = r_{Cav} - \cos(\varphi_0 + \delta\varphi(\theta)) \quad (4.7)$$

$$y_{Cav}(\theta) = r_{Cav} - \sin(\varphi_0 + \delta\varphi(\theta)) \quad (4.8)$$

These exact expressions for the position of the monitor axis can now be developed for small $\delta\varphi(\theta)$:

$$x_{Cav}(\theta) = r_{Cav} - \cos(\varphi_0) - r_{Cav} - \sin(\varphi_0)\delta\varphi(\theta) + O(\delta\varphi^2(\theta)) \quad (4.9)$$

$$y_{Cav}(\theta) = r_{Cav} - \sin(\varphi_0) + r_{Cav} - \cos(\varphi_0)\delta\varphi(\theta) + O(\delta\varphi^2(\theta)) \quad (4.10)$$

Using equations 4.4 and 4.5 and neglecting $O(\delta\varphi^2(\theta))$, one finds approximately:

$$\bar{x}_{Cav}(\theta) = x_0 - r_{Cav} - \sin(\varphi_0)\delta\varphi(\theta) \quad (4.11)$$

$$\bar{y}_{Cav}(\theta) = y_0 + r_{Cav} - \cos(\varphi_0)\delta\varphi(\theta) \quad (4.12)$$

Now the θ -dependence is written out with equation 4.6:

$$\bar{x}_{Cav}(\theta) = x_0 - r_{Cav} - \sin(\varphi_0) - \arctan\left\{\frac{\Delta h_0 - \cos\theta}{d_0}\right\} \quad (4.13)$$

$$\bar{y}_{Cav}(\theta) = y_0 + r_{Cav} - \cos(\varphi_0) - \arctan\left\{\frac{\Delta h_0 - \cos\theta}{d_0}\right\} \quad (4.14)$$

For $\Delta h \ll d_0$ $\arctan(x) = x + O(x^3)$ holds and the amplitudes Δx and Δy can be identified:

$$\Delta x = r_{Cav} - \sin\varphi_0 - \frac{\Delta h_0}{d_0} \quad (4.15)$$

$$\Delta y = r_{Cav} - \cos\varphi_0 - \frac{\Delta h_0}{d_0} \quad (4.16)$$

Thus, the expressions of the monitor position are:

$$\bar{x}_{Cav}(\theta) \sim x_{0Cav} - \Delta x - \cos(\theta) \quad (4.17)$$

$$\bar{y}_{Cav}(\theta) \sim y_{0Cav} + \Delta y - \cos(\theta) \quad (4.18)$$

The maximum difference $x_{Cav} - \bar{x}_{Cav}$ is 4 μm , so that a sinusoidal movement was assumed in the following. If the dimensions due to the adjustment ($d_0 = 470$ mm, $x_{0Cav} = 225$ mm and $y_{0Cav} = 211$ mm) are used, the following is found $\Delta x = 1.63$ mm and $\Delta y = 1.74$ mm.

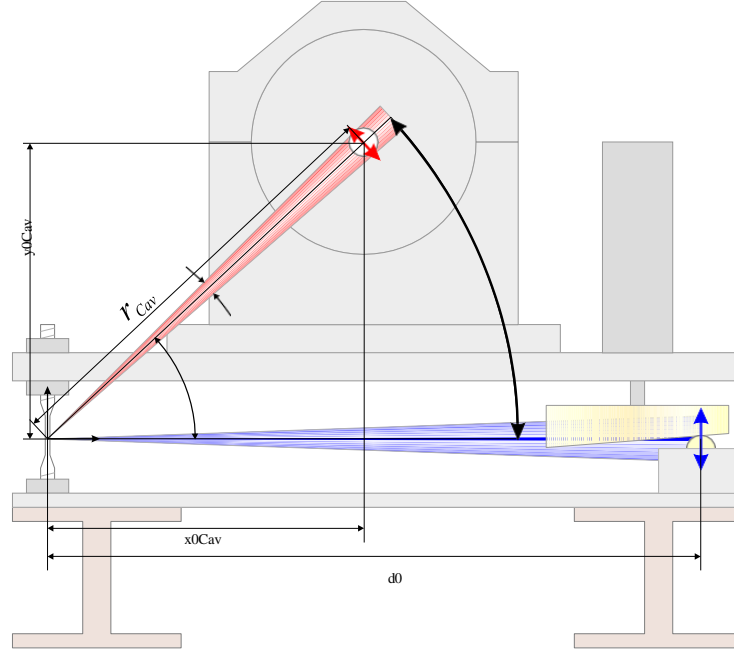


Figure 4.3.: Sketch for calculating the stroke in x- and in y-direction

4.1.2. Calibration of the lifting mechanism

After production and initial mechanical tests in the laboratory, the lifting mechanism was installed in the beamline. Dial gauges were used for calibration (see Fig. 4.1 (b)), with the help of which the position of the resonator in the x- and y-direction could be determined with an accuracy of 5 μm depending on the angle of rotation of the swash plate.

A stop-free rotary potentiometer (marked green in Figure 4.6) attached to the gearbox axle below the swashplate was used to display the angle.

The measurement points shown in figure 4.4 were measured over two revolutions of the swash plate (pass (a) and (b)) in order to detect possible misalignments. As shown in equations 4.17 and 4.18, the measuring points can be fitted very well by sinusoidal curves:

$$y = y_0 + \Delta y_0 - \cos(k_\Omega R + \varphi)_0 \quad (4.19)$$

with y_0 [μm] as the additive constant, Δy_0 [μm] as the amplitude of the movement, the angle parameter $k_\Omega = 2\pi/R_0$ [$1/\Omega$] and φ_0 as the phase correction. The average deviation of the measuring points in x- and y-direction is 5 μm . The amplitudes determined in this way

$\Delta x_0 = 1.67$ mm and $\Delta y_0 = 1.71$ mm agree to about 2 % with the values of Δx and Δy calculated according to equations 4.15 and 4.16.

4. calibration of an HF position

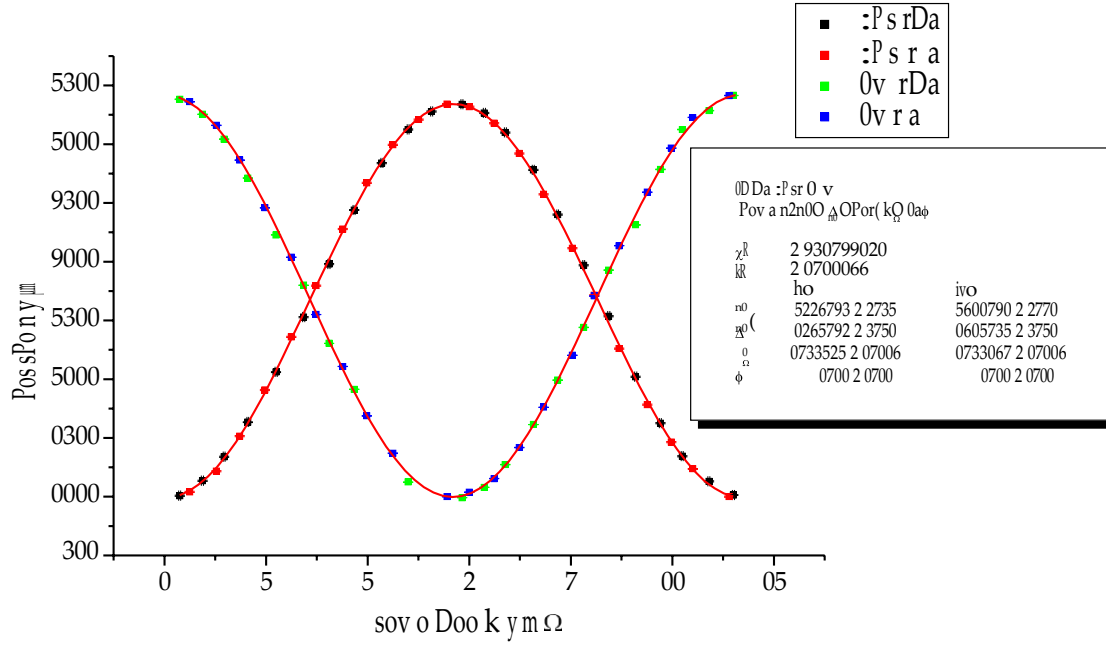


Figure 4.4: The horizontal and vertical positions are shown as a function of the swash plate angle (measured with a rotary potentiometer).

4.1.3. Bending of the tapered threaded bolts

As mentioned above, the two threaded bolts were turned to reduce the required bending force. It should be shown here that the turning has a positive effect on the force balance.

According to [Dub01], the moment of rotation required to bend a cylindrical bolt is M (α , r , L):

$$M(\alpha, r, L) = \frac{2\alpha}{L} E_{Eisen} - I_r(r) \quad (4.20)$$

This requires the 2nd order surface moment:

$$I_r(r) = \frac{\pi r^4}{4} \quad (4.21)$$

If the modulus of elasticity $E_{Eisen} = 211 \cdot 10^9$ Pa, the radius $r = 3$ mm and the length $L = 30$ mm are used, this additional restoring torque is as follows
 $\alpha_{max} = \delta\phi_{max} = 0.44^\circ$ maximum $M(\alpha_{max}, r = 3 \text{ mm}, L) = 6.9$ Nm per bolt in the ver-
equal to $M(\alpha_{max}, r^t = 6 \text{ mm}, L) = 110.4$ Nm *without* turning. With $F_{(bolt)} = M/d_o$
the swash plate is subjected to an additional load of max. 14.7 N per
screw to it. However, this amount is negligible compared to the uncertainty of the
moving mass.

4.1.4. Load on the gearbox

Radial forces

In the following estimation, a constant force on the swash plate over time was assumed, whereby the maximum force caused by the threaded bolts was accounted in F_o according to Equation 4.22. The maximum force acting on the swash plate is

$$F_o \sim \frac{1}{2} \cdot m_o \cdot g + 2 \cdot F_{(bolt)} \quad (4.22)$$

is 200 N for a total weight of $m_o \sim 37$ kg. The factor¹ in Gleichung 4.22 accounts that the swash plate only has to carry about half² of the weight, the other half is carried by the screws, since the HF monitor is located approximately above the centre of the base plate. Due to the inclination of the swash plate, this bearing force causes a component of

$$F_{\perp} = F_o \sin \varepsilon \quad (4.23)$$

of 14.5 N parallel to its sloping underside. The torque caused by F_{\perp}

$$M = \vec{r} \times \vec{F}_{\perp} \quad (4.24)$$

of 0.44 Nm must be absorbed by the bearing of the gear shaft, whereby the maximum permissible radial torque on the axle is specified as $M_{max} = 1.68$ Nm (blue force vectors in figure 4.5).

Tolerances

The problem of the mechanical overdetermination of the system is not critical, despite the rigid attachment to the axle and the two bearing points. On the one hand, the unevenness of the swash plate is very small ($<50 \mu\text{m}$) due to the production on the lathe, and on the other hand, a maximum radial play $\Delta x = 0.14$ mm (5 mm from the gearbox output) is specified for the gearbox. This radial backlash leads to an angular backlash of

$$\Delta \alpha = \arctan \left\{ \frac{\Delta x}{L_1 + 5 \text{ mm}} \right\} \quad (4.25)$$

of 0.3° (red horizontal arrow in figure 4.5). This game in turn is expressed at the upper ball bearing in a permissible clearance

$$\Delta y = \sqrt{(L_1 + L_2)^2 + r^2} \cdot \sin \Delta \alpha \quad (4.26)$$

The value for Δy (red vertical arrow in figure 4.5) is therefore 0.38 mm and is certainly not exhausted.

¹pessimistic assumption: $L_1 = 1/2 L_o$; gear shaft is fixed in the middle of the gearbox without tolerance (Figure 4.5).

4. calibration of an HF position

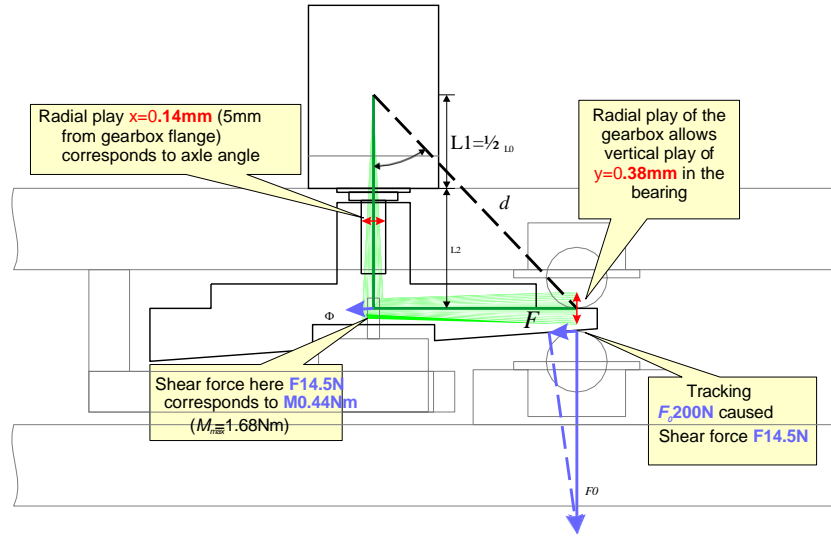


Figure 4.5: Transverse forces and tolerances occurring in the system due to axial play

4.1.5. Engine power

Before the final production, calculations were made for the dimensioning of the motor and gearbox. The potential energy as a function of time is as follows

$$E(t) = \int_0^{-t} F_0 - ds = \int_0^{-t} F_0 - \frac{dh}{dt} dt = \int_0^{-t} F_0 - h'(\theta) dt \quad (4.27)$$

The derivative with respect to time gives the required power as a function of time:

$$P(t) = \frac{\partial E(t)}{\partial t} = \frac{\partial}{\partial t} \int_0^{-t} F_0 - h'(\theta(t)) dt = F_0 - h'(t) \quad (4.28)$$

The time dependence of h is obtained by substituting $\theta = \omega t$ into equation 4.3, where ω is the angular velocity of the swash plate:

$$h(t) = \Delta h_0 - \cos(\omega t) \quad (4.29)$$

$$\Rightarrow h'(t) = -\Delta h_0 - \omega \sin(\omega t) \quad (4.30)$$

Thus one obtains for the output

$$P(t) = -F_0 - \Delta h_0 - \omega \sin(\omega t) \quad (4.31)$$

The drive must achieve the highest power at time $t_0 = \frac{3\pi}{2\omega}$ ($\frac{\partial}{\partial \omega} P(t) = 0$ for $\frac{\partial}{\partial t} P(t) = 0$); $P(t = t_0) \sim 4.6 \text{ W}$ at an orbital frequency of 1 Hz. The gearbox is equipped with

4.2 Calibration of the signals during beam

a maximum efficiency $\eta = 70\%$, whereby the minimum power to be demanded of the motor with a safety distance should be between 7 and 8 W. In later operation, the motor was supplied with a voltage of 12 V. The maximum current consumed during operation was just under 1 A. The maximum current I_{max} consumed during operation reached just under 0.6 A, which confirms the estimate above.

4.2. Calibration of the signals during beam operation

4.2.1. Setting the reference phase

Before starting a measurement with an RF monitor, it must always be checked whether the phase of the reference signal matches the phase of the beam (see figure 3.5 (b)) and corrected if necessary. For this purpose, non-critical diagnostic pulses are generally used, which are *not* shot through the centre of the monitor. The reference phase is now varied until the signal is at a maximum.

However, a misadjustment of the nominal phase is only cosinusoidal in the calibration, which means that small deviations from the ideal phase initially have only a minor effect.

4.2.2. Calibration with c.w. beam

Calibration is very simple here. The desired beam current is set and the mechanics are set in motion. After only one revolution of the swash plate, a complete calibration is available, which can be stored with the oscilloscope. In order to reduce the statistical error and to limit the influence of the unavoidable beam position fluctuations, the averaging was extended over several runs. The results are already shown in Figure 3.7.

4.2.3. Calibration with diagnostic pulses

In beam operation with diagnostic pulses, calibration proceeds differently. The integral over the pulse from its start to the zero crossing serves as a measure of the signal size.

Since the signal is now a pulse and is not continuous, individual signals have to be pulse trains are digitised as a „snapshot“. In order to obtain sufficiently good statistics, at least 100 such „snapshots“ must be taken, which are later analysed offline. However, because this process takes some time (one „snapshot“ per revolution) and the beam drifts away a little at a time, the sensitivity error (represented by the coefficient a [1/mm]) is in figure 3.11) is normally somewhat larger than in c.w. operation.

The result of such a calibration is already shown in Figure 3.11.

4. calibration of an HF position

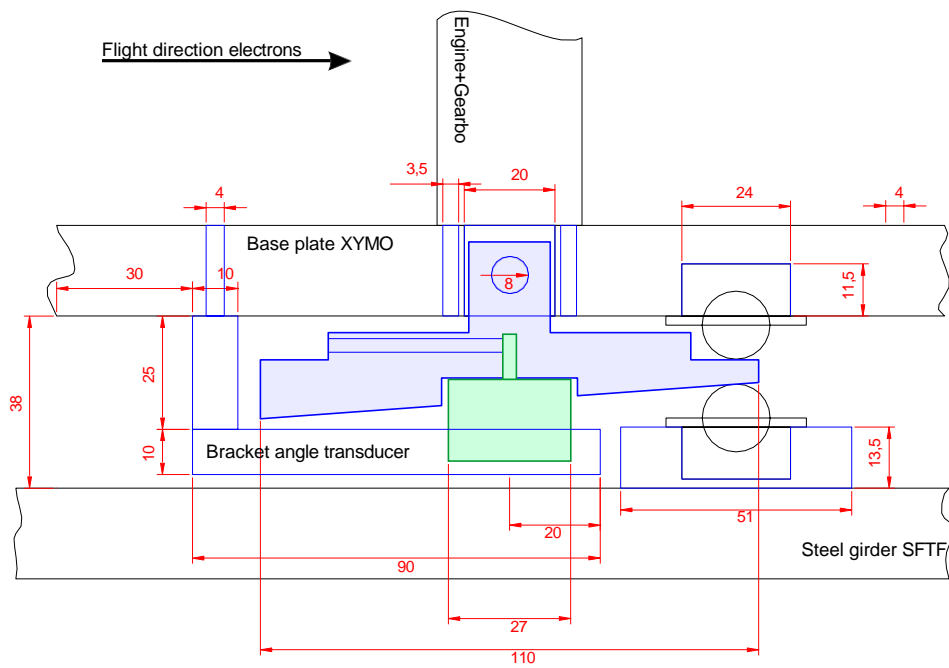


Figure 4.6.: View of the lifting mechanism from the side, dimensions in millimetres, at Parts to be manufactured and bores are marked in blue, eccentric and rotary potentiometer are filled in.

4.2 Calibration of the signals during beam

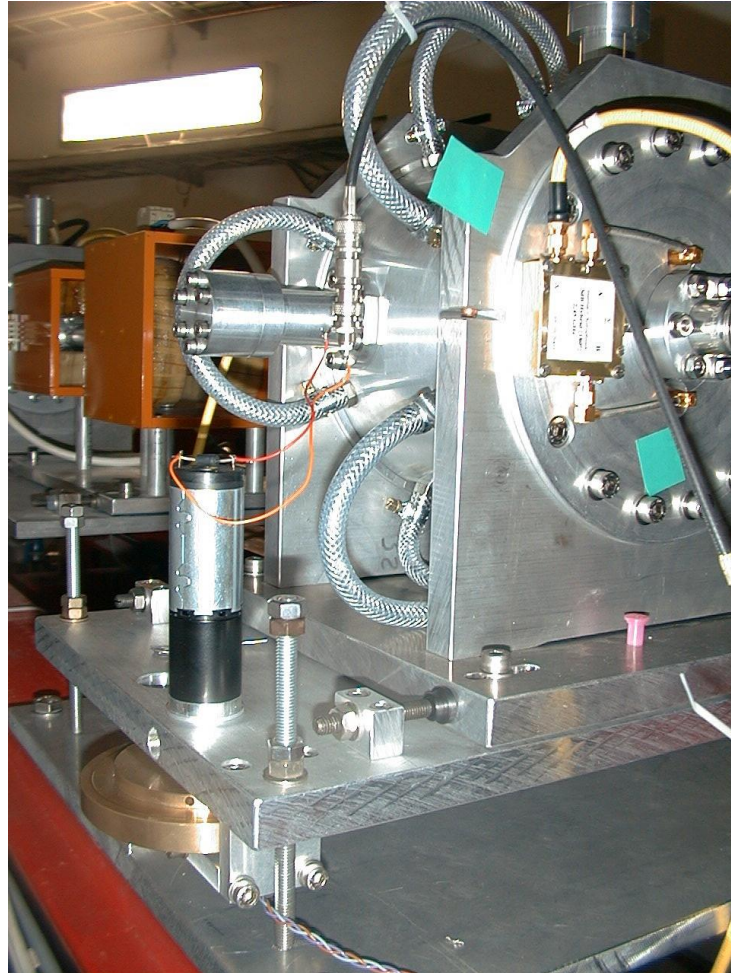


Figure 4.7.: Finished calibration mechanism from XYMO14: on the left, made of brass, the swash plate can be seen.

5. COBRA multiplexer

5.1. Introduction to the previous system

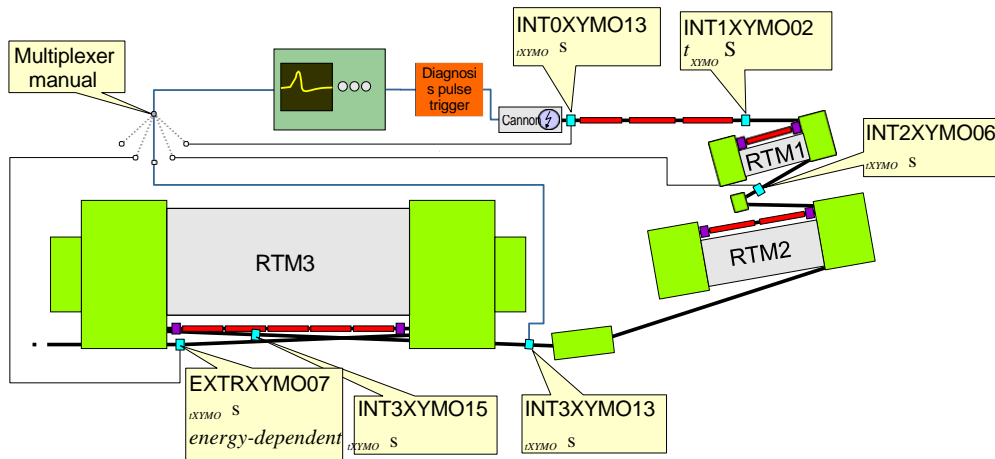


Figure 5.1: Sketch of the positioning of the RF monitors from the cannon to the extraction (855 MeV). In addition, the different travel times of the beam from the cannon to the respective position are indicated.

The following chapter is devoted to improving the diagnostic capability in connection with the diagnostic pulses.

Role model: the microtrone

In the microtrons, the diagnostic pulses on the linac axis are detected by „low-Q” monitors, whose time constant T_{Signal} is not very high due to the low loaded rate.

of about 40 is in the order of a few nanoseconds and thus only slightly longer than the circulation time in the smallest microtron. When such a pulse flies through, it generates n temporally posterior pulses in each of the monitors mounted there.

pulses, where n is the number of revolutions (Figure 5.2 (b)). If, for example, the direction of the beam is changed in a cycle, the reaction of the beam can be changed in the following way

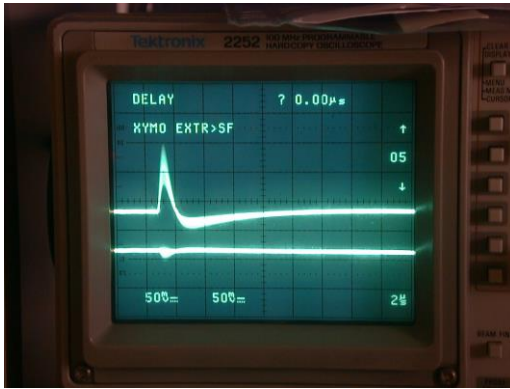
The following recirculations can be observed in a very simple way.

The current situation in the beamlines

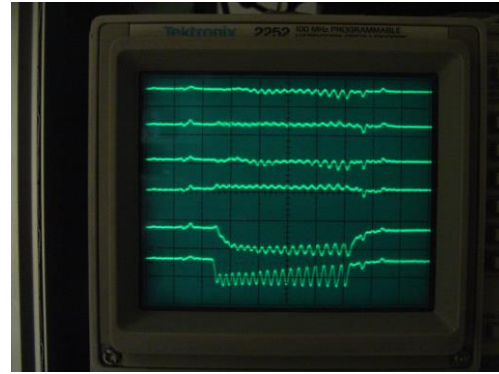
In the injector linac as well as in the beam delivery systems between the microtrons and behind the RTM3, „high-Q” monitors are used in order to be able to detect even small

c.w.

5.1 Introduction to the previous system



(a) typical signal of an RF monitor in the slide-intensity diagnosis pulse mode: The signal is active until the first zero crossing 2 to 3 μ s long.



(b) 4 deposition as well as phase- and signal of the RTM1. The signals of the low-Q"-HF-Monitors need to be shorter than the time for one revolution (~ 20 ns)

Figure 5.2.: Diagnostic pulses on the operating oscilloscope (photo)

intensity and position of the beam. When operating with diagnostic pulses, a signal of up to 10μ s is obtained, the maximum value of which is approximately proportional to the beam deposition.

With the help of the multiplexer, any monitor can be selected and its x and y signals displayed on an oscilloscope in the control room (figure 5.2 (a)). This is shown schematically in figure 5.3: The pulse trigger simultaneously triggers the oscilloscope so that the signal of the selected xy monitor appears on the oscilloscope after the electron beam has passed through the accelerator.

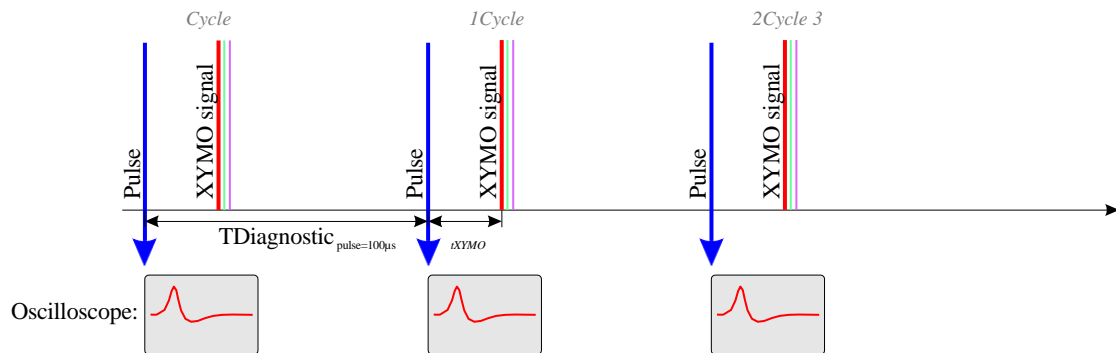


Figure 5.3.: Pulse trigger and signals (old system)

In order to reduce the time for the adjustment and correction of the beam and to be able to better analyse occurring errors such as the instability of beam guiding components, a simultaneous display of all XYMO signals of a beam guiding section was required. Since delay lines are not suitable due to the large

5. COBRA multiplexer

signal lengths of a few μs are impracticable, the system described below was constructed according to a suggestion from the ^{MAMI} operating group¹.

5.2. Technical parameters

5.2.1. Control of the multiplexer

For parallel display, the manually controlled multiplexer first had to be controlled more quickly so that well-timed switching between the individual monitors of a beamline section was possible.

This made it possible to observe a number of signals simultaneously mixed (figure 5.4).

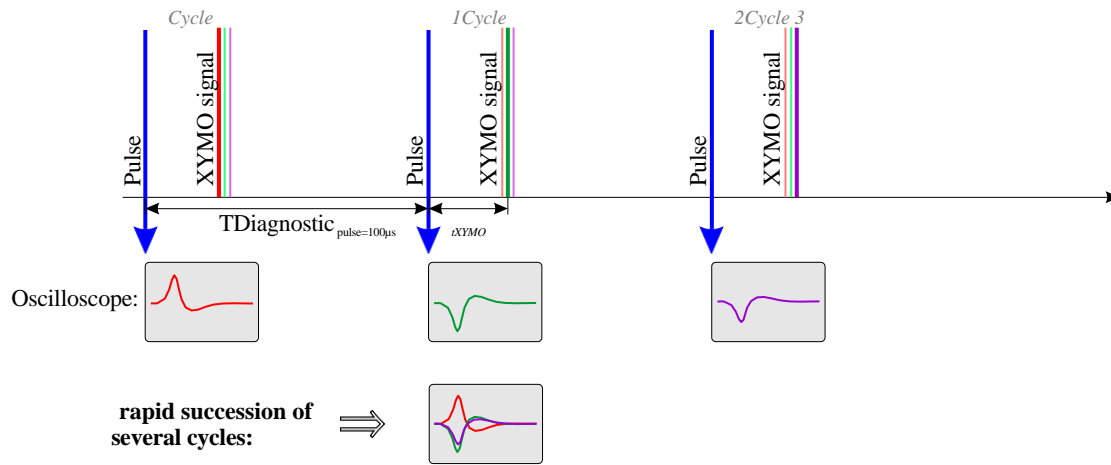


Figure 5.4.: Pulse trigger and signals (automatic channel switching only)

The electronics of the multiplexer are capable of changing channels at most every 100 μs . However, the *control system* is not designed to address the multiplexer so quickly and regularly. Here, the original multiplexer was to be expanded by controlling the channel selection with the aid of a second system. This system was to be freely programmable and later only receive information from the control system as to which group of RF monitors was to be switched through alternately.

5.2.2. Triggering the oscilloscope

In order to separate the signals optically, it is necessary to assign individual trigger times for the oscilloscope to each monitor of a group.

The t_{Signal} length of the individual signals to be displayed is approximately 3 μs . To ensure that the quality of the display does not suffer from the jitter of the trigger time,

¹J. Müller: *private communications* 2003

an upper limit of 10 % of the signal length was continued.

$$\Delta t_{\text{Jitter}} \approx T_{\text{Signal}} \quad (5.1)$$

A microprocessor system based on a RISC processor was ordered from *SenTec* (Motorola ColdFire MCF 5272 with 66 MHz clock rate corresponding to a clock duration of 15 ns). On the one hand, the base board offers serial V24 connections, via which communication with the control system could be handled in a simple manner. On the other hand, external port lines as well as interrupt lines are available, which are wired directly to the processor, whereby a safe triggering of the oscilloscope should be achieved. Parallel to triggering, this module was also equipped with an interface to the multiplexer.

The delay required for any *xy monitor* depends on the transit time of the electrons from the gun to the monitor as well as on the desired position of the signal train on the oscilloscope:

$$\Delta t_{\text{Trigger}}(xy) = T_{\text{Diagnostic pulse}} + t_{XYMO}(xy) - t_{Osz}(xy) \quad (5.2)$$

Here $\Delta t_{\text{Trigger}}$ (see figure 5.5) is the required delay of the trigger in relation to the original pulse trigger, $T_{\text{Diagnostic pulse}}$ is the time between two consecutive pulses, t_{XYMO} is the transit time of the electrons from the gun to the corresponding monitor and t_{Osz} is finally the position on the oscilloscope.

In order to separate the individual pulse signals, the oscilloscope should be triggered individually for each monitor to be displayed. This should give the impression of a simultaneous display, similar to the microtone signals (fig. 5.5).

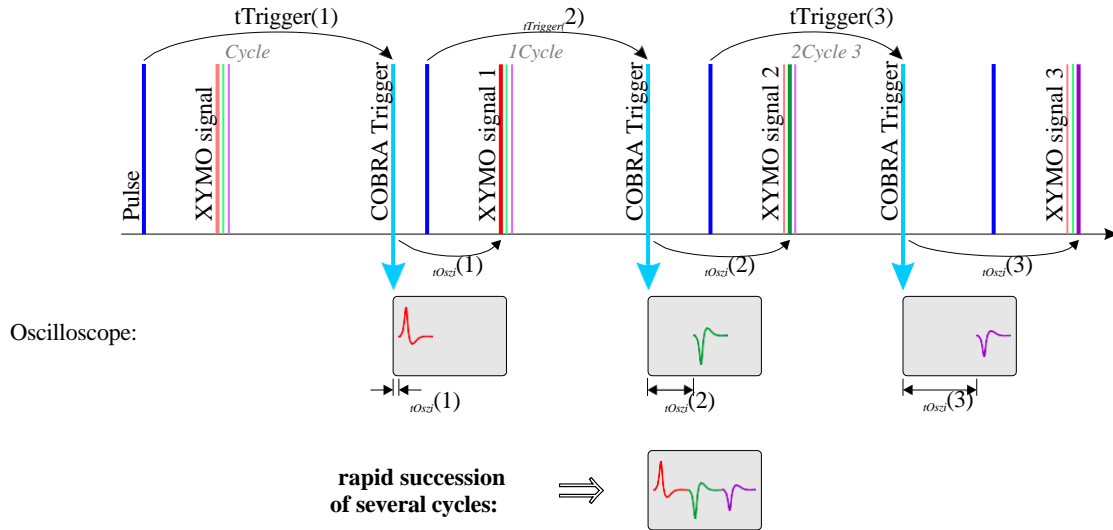


Figure 5.5.: Pulse trigger and signals (automatic switching and triggering)

5.3. Jitter study

The first examination of the module concerned the jitter (Figure 5.6). It turned out that there are two accumulation points that are about 230 ns (corresponding to 14 clock cycles) apart and that the width of the accumulation points is about 50 ns. The entire distribution is even slightly more than 800 ns wide, but the ratio of signal to background is sufficient.

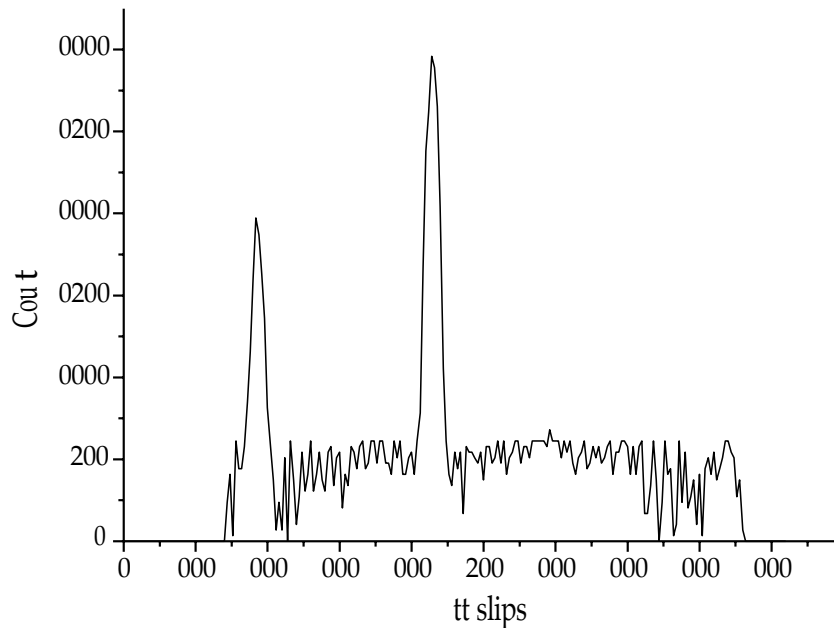


Figure 5.6.: A histogram of the duration times recorded over 10^5 trigger cycles is shown, the time zero point is arbitrary.

Attempt to explain the jitter distribution

Detailed information on the timing of the ColdFire processor can be found in [MCF98]. In summary, the reason for the non-constant response time is probably that the processor waits in a small loop until an interrupt is triggered by the pulse trigger. In order to process the interrupt, this loop must be interrupted, the state of the registers on the stack must be saved and the interrupt must be handled. Depending on the history, this process can lead to the cache controller having to load program code from the slower SD-RAM into the cache (which means a time delay) before they can be executed. However, this problem could in principle be avoided by using a ^{DSP}² instead of a microprocessor system, in which all instructions are executed in a time-defined manner under all circumstances. However, the construction of a DSP system was dispensed with for reasons of cost.

²DSP: Digital Signal Processor

5.4. Structure of the COBRA add-on module

5.4.1. Hardware

The COBRA add-on module to the multiplexer was built up from various components:

- Communication with the control system should take place via the serial UART.³ - interface of the base board by means of a hardware interrupt.
- The pulse trigger was placed directly on an EXT interrupt line of the processor and should also generate a hardware interrupt.
- The switching of the multiplexer should be done with the help of a circuit that should be addressed via the GPIO port outputs of the processor.⁴ -port outputs of the processor.
- The trigger signals should also be generated via the GPIO port outputs of the processor.
- For the blanking of the oscilloscope, a separate hard-wired delay circuit was designed, which was also to be triggered by the GPIO port outputs of the processor.

Figure 5.7 illustrates this with a graphical overview.

5.4.2. Software

The software for the COBRA system is divided into two parts. On the control system side there is a service routine that controls and monitors the COBRA system. There, in turn, the actual multiplexer programme runs, which controls the switching of the channels and generates the trigger signals.

Initialisation

When the system is initialised, the control system process automatically resets the board. This starts the factory-installed firmware dBUG [DBG99]. The control system process now causes the firmware to download and start the actual multiplexer programme via the serial V24 interface. The system is now ready for use.

a) Control system process

If a beamline section is to be displayed, the control system process sends the necessary data (multiplexer ~~data~~ delay times) to the multiplexer programme. This data is located in the corresponding database entries of the control system database and can be flexibly edited there.

³UART: Universal Asynchronous Receiver and Transmitter

⁴GPIO: General Purpose Input Output

5. COBRA multiplexer

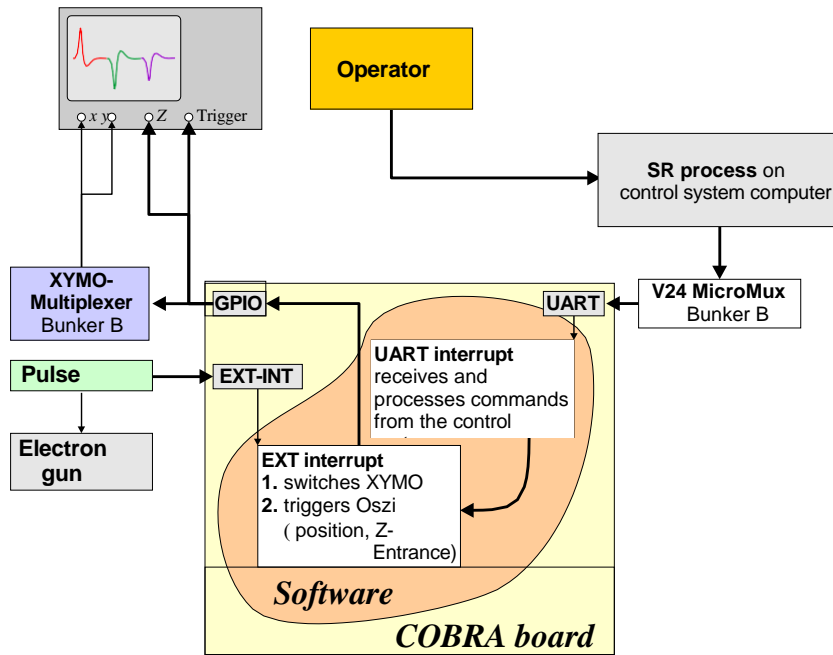


Figure 5.7.: Block diagram of the COBRA system

b) COBRA process

The multiplexer software on the COBRA system waits in an infinite loop until one of the following events occurs:

UART interrupt: Commands and data from the control system are written character by character into a buffer of the programme until an end of line has been sent. The command is then processed.

EXT interrupt: Only if the system has been activated, the multiplexer is switched and the oscilloscope is triggered accordingly.

5.5. The result

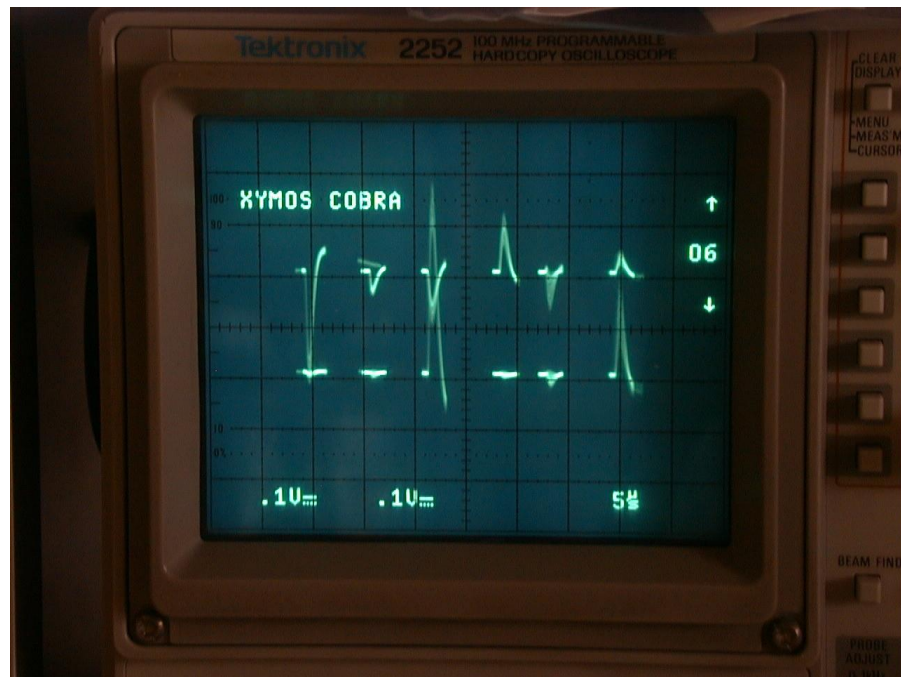


Figure 5.8.: xy-monitors of the SFTF beamline (top horizontal, bottom vertical signals)

Figure 5.8 shows the finished result. Here the six HF position monitors of the beamline (see figure 2.1) can be seen.

6. summary

6.1. Beam optical measurement

From the results of the adaptation of the model to the measured matrix, the required excitation str"ome can now be recalculated in connection with the individual quadrupole models in order to come closer to the nominal setting of the system. For time reasons, this could not be checked within the framework of the present work.

In addition, an automated routine can be developed to determine the transfer matrix of this subsection in a short time.

In addition to measuring the T2 section, it is also desirable to systematically investigate the section from QUAD02 to QUAD06 (T1 section). However, this ~~requires~~ additional correction magnets and HF position monitors.

Devices used

To measure the optical radiation properties, the signals from the RF position monitors were digitised with a Tektronix oscilloscope (TDS3014B). **T h i s** oscilloscope allows automated use and can also carry out manipulations on the signal to be stored. The main method used was averaging over 2^n trigger events (n natural number).

6.2. HF position monitors

The results presented here show that the mechanics described in chapter 4 are very well suited for performing precision investigations on the electron beam. This means that this instrument is also a good way of ensuring that the position signals of the position monitors actually indicate realistic deposition values during the evaluation, such as the current A4 experiment on parity violation, and do not reach non-linear ranges due to a poor reference wave phase.

Suggestions for improvement in the case of new construction:

- The bearing of the swash plate should be reconsidered in order to reduce the load on the gearbox.
- The gear should be driven by a worm from the motor so that the monitor can stop at the desired position.

- If a worm gear is used, it is advantageous to have a motor
The monitor can then be moved „by hand" via this shaft.

Open questions about the HF position monitors:

- 1. Diagonal movement during calibration:** Since the movement of the monitor is carried out „diagonally", i.e. an *x-position* always goes hand in hand with a *y-position*, the following would apply
it makes sense to investigate whether the monitor reacts differently with regard to the calibration character after a 43.2° rotation.
- 2. Influence of the mode stabilisers:** The influence of the mode stabilisers on the TM_{110} mode has not been investigated in detail. Does the field deform when the mode is excited diagonally? An investigation *without* the stabilisers should provide clarity here.
- 3. Higher frequency components:** The influence of higher frequency components on the measurement electronics has not been systematically investigated. The non-linear effect could well result from a rectification of undesired signal components.

6.3. The COBRA multiplexer

The display of several HF monitors on the operating oscilloscope is based on its ability to influence the brightness of the signal curve (*Z input*). To display *n* monitor signals, the oscilloscope must be triggered *n times*. This means that the zero line is drawn just as often and thus appears correspondingly brighter. Unfortunately, this possibility of brightness modulation is not available with most digital oscilloscopes.

Acknowledg

The present work was carried out from May 2003 to May 2004 at the Institute for Nuclear Physics of the Johannes Gutenberg University.

I would like to thank Professor Dr. Th. Walcher for making the diploma thesis possible in his accelerator working group. I am particularly grateful to Dr. K.-H. Kaiser, who was always available as a competent contact person.

Furthermore, I would like to thank all members of the accelerator working group for their helpful support and pleasant working atmosphere, especially H. Euteneuer, F. Fichtner, B. Gutheil, A. Jankowiak, P. Jennewein, W. Klag, H.J. Kreidel, U. Ludwig-Martin, J. Müller, A. Nuck, J. Röhren, S. Schumann, B. Seckler, M. W. T. Zschocke, and K. Aulenbacher.

I would also like to thank all the members of the institute who helped me with my work. Special thanks go to Mr. Jung from the mechanical workshop, who was constructively involved in the development of the lifting mechanism.

Special thanks go to Monika Weis for her support during the preparation of this thesis. I would also like to thank my family, as they made it possible for me to study at all.

Marco Dehn, May 2004

Part IV.

Appendix

A. Correction magnets

In order to determine the matrix of a system, it must be known exactly which deflection the beam experiences when passing through a correction magnet (Wedler).

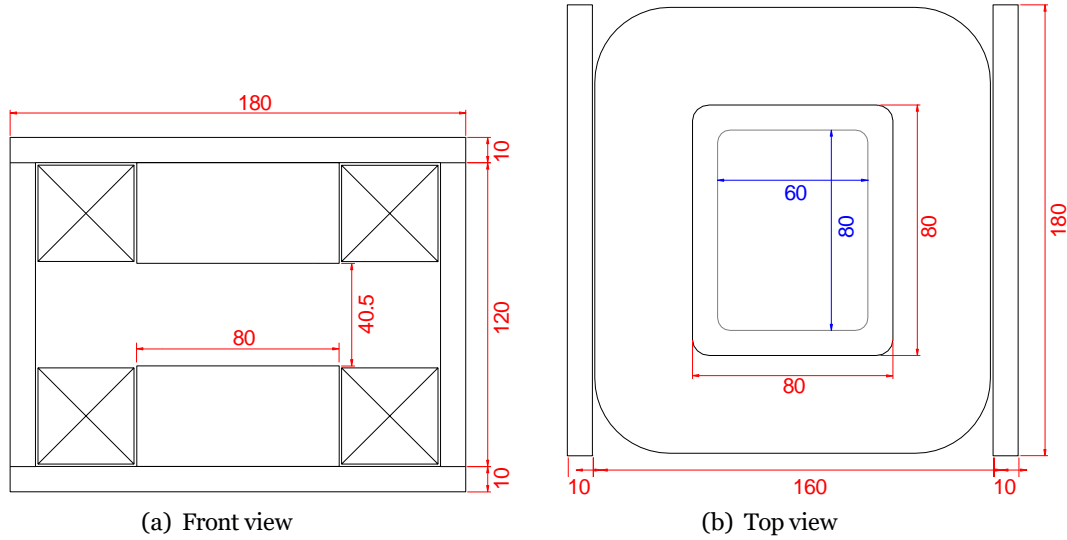


Figure A.1: Sketch of the used wedler type 1. For type 2, the area of the pole shoe has been reduced to 80x60 mm² (blue) (iron body made of bright steel ST37).

There are two types in use, which differ in their coil dimensions (Type1 with 2.4 Ω at 100x80 mm² pole piece and Type2 with 1.2 Ω at 80x60 mm² pole piece).

Field maps were prepared for both types of wedge at set currents of 0, 1, 2, 3 and 4 amperes (see figure A.2). With the help of these field maps, the deflection angle ϑ_0 can be determined from the longitudinal sections along the beam axis. From the Lorentz force, one obtains for this purpose:

$$\vartheta_0(i) = \frac{e}{p} \int B(i) \cdot ds = \frac{e}{p} \int B(i) \cdot L_{eff} \quad (A.1)$$

with the maximum magnetic field $B_0(i)$ along the integration path:

$$B_0(i) = a_0 + a_1 \cdot i + O(i)^2 \quad (A.2)$$

In particular, the coefficient a_0 depends very much on the history of the wedler, maximum values of 20 Gauss were measured. In order to generate a prehistory as well defined as possible in a simple way, the wedler was first driven to +4 A, then to -4 A and then to zero for 200 ms before setting the desired deflection angle. In order to

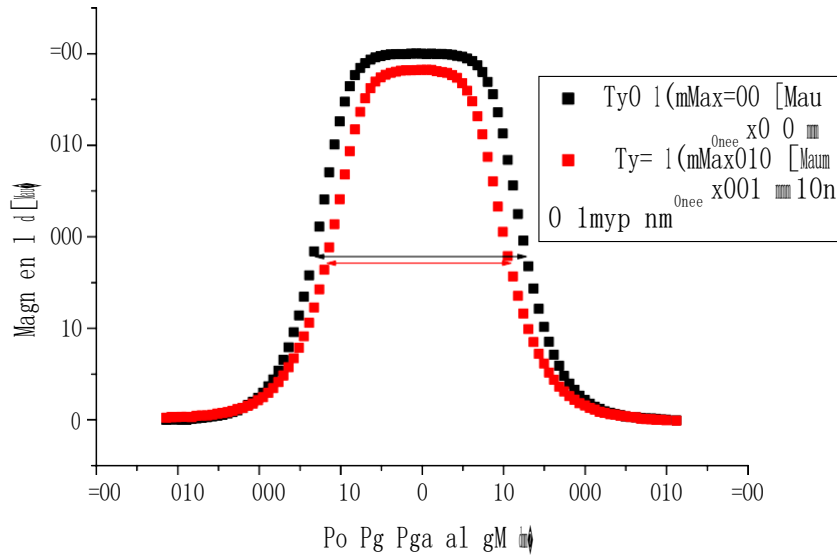


Figure A.2.: longitudinal field curve at 1 Amp`ere

To verify the improvement of this cycling procedure, two measurements were made on the beam, with the wedler setting diced values before each adjustment of the reference angle: One measurement used the „cycling” procedure, the second measurement did not. In comparison, cycling reduced the dispersion of $\theta_0(0)$ (and thus of B_0 and a_0) by one order of magnitude (see figure A.3). For this measurement and also during the beam tests

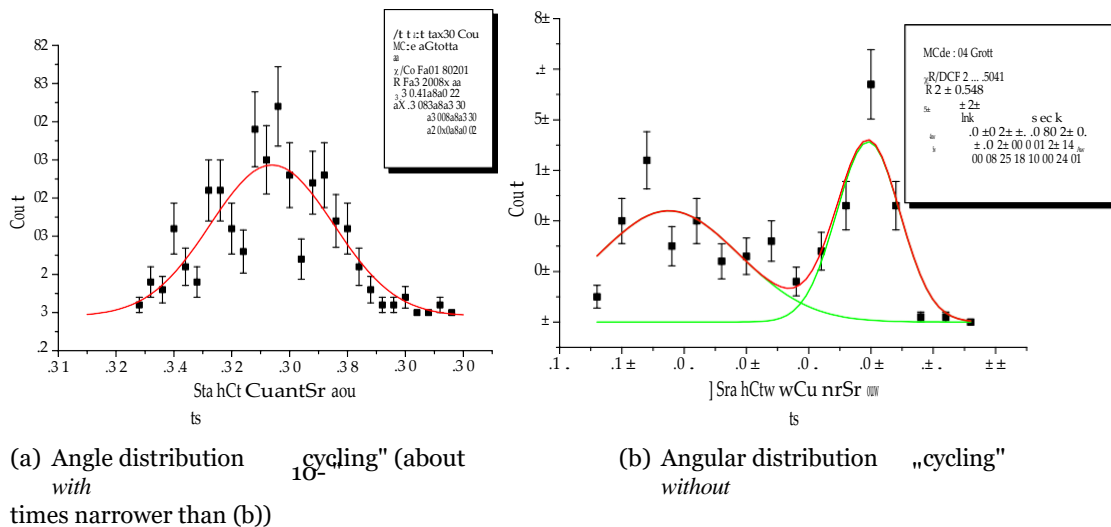


Figure A.3.: Effect of Wedler- cycling".

a pause of 200 ms was chosen so that the cycling procedure did not take too much time. Longer waiting times (a few seconds) in the laboratory, however, brought an improvement by almost two orders of magnitude (albeit with a poor statistic of only 10 values).

A. Correction magnets

Influence of misalignments

To determine the influence of small misalignments of the welders on the deflection angle, ϑ_0 was determined not only along the beam axis, but also up to a distance of 12 mm to the left and right of it (figure A.4).

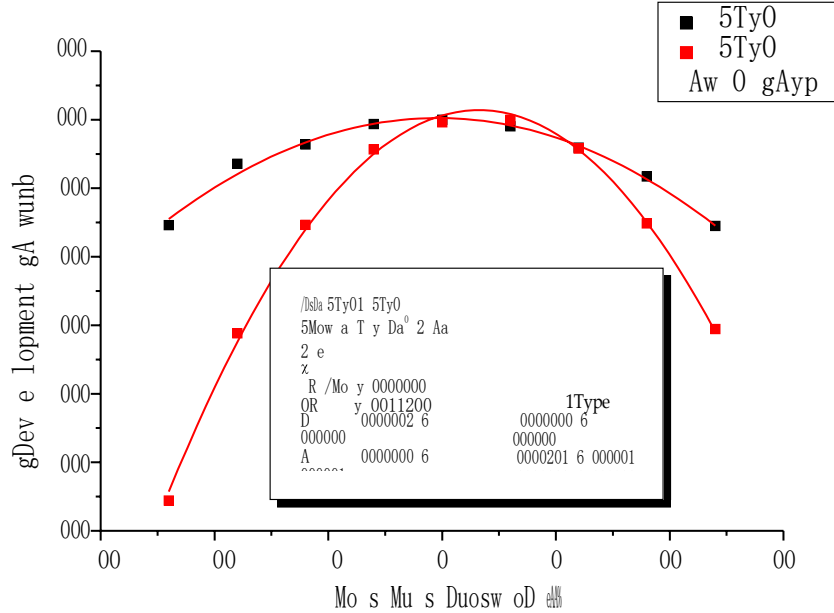


Figure A.4.: Deviation of the deflection angle (transverse) at 1 Amp`ere

One has to supplement equation A.1 with the transverse dependence (as shown in figure A.4) to this effect account:

$$\vartheta(i, x) = \vartheta_0(i) - (1 - \delta - x)^2 \quad (\text{A.3})$$

The value for δ is $5.1 \cdot 10^{-5} \text{ mm}^{-2}$ for type 1 and $10.4 \cdot 10^{-5} \text{ mm}^{-2}$ for type 2. This means that the amount of the deflection angle for type 1 decreases by 0.5 % 10 mm from the axis, but for type 2 it already decreases by 1 % (see figure A.4).

A.1. Compilation of the most important data

The deflection angle $\vartheta(i)$ was determined from the longitudinal profiles for each current strength. The slope of the straight line in Figure A.5 corresponds to the sensitivity ϑ_0 . Since the additive constant depends on the respective history of the material, it is not listed in Table A.1.

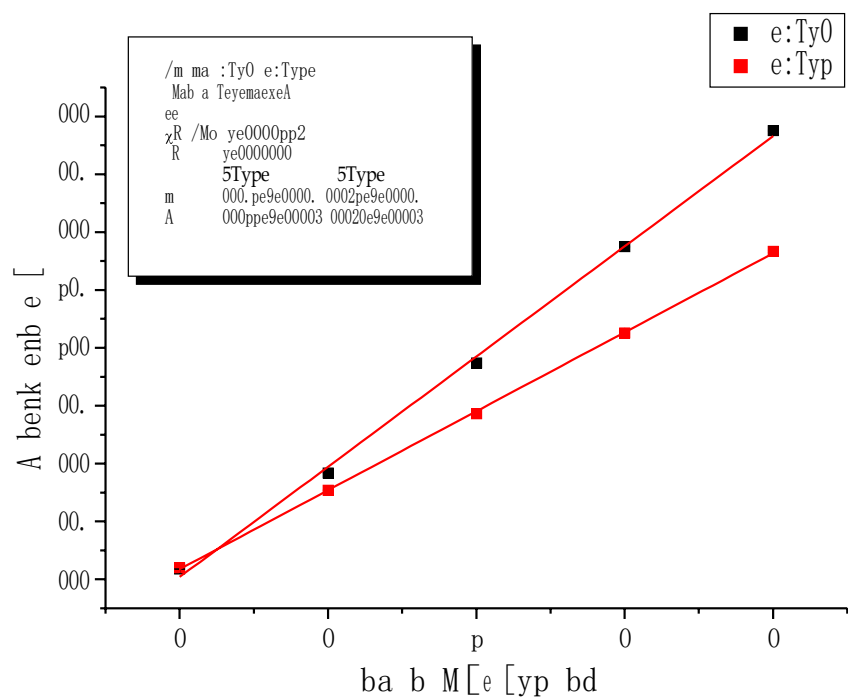


Figure A.5.: Deflection angle of the wedler, determined over seven longitudinal profiles

Table A.1.: List of Wedler data

	Type1	Type2
θ [mrad/A]	0.952 ± 0.015	0.682 ± 0.015
δ [mm ⁻²]	$5.1 \cdot 10^{-5}$	$10.4 \cdot 10^{-5}$

B. Quadrupole

B.1. Simple Checking the strength of a quadrupole

In the section of the beamline system to be investigated (see Figure 2.1), quadrupoles from the companies Bruker and Danfysik are used. Their technical data (aperture, number of turns, effective field length) are very similar, but the excitation curves are quite different (see figure B.1).

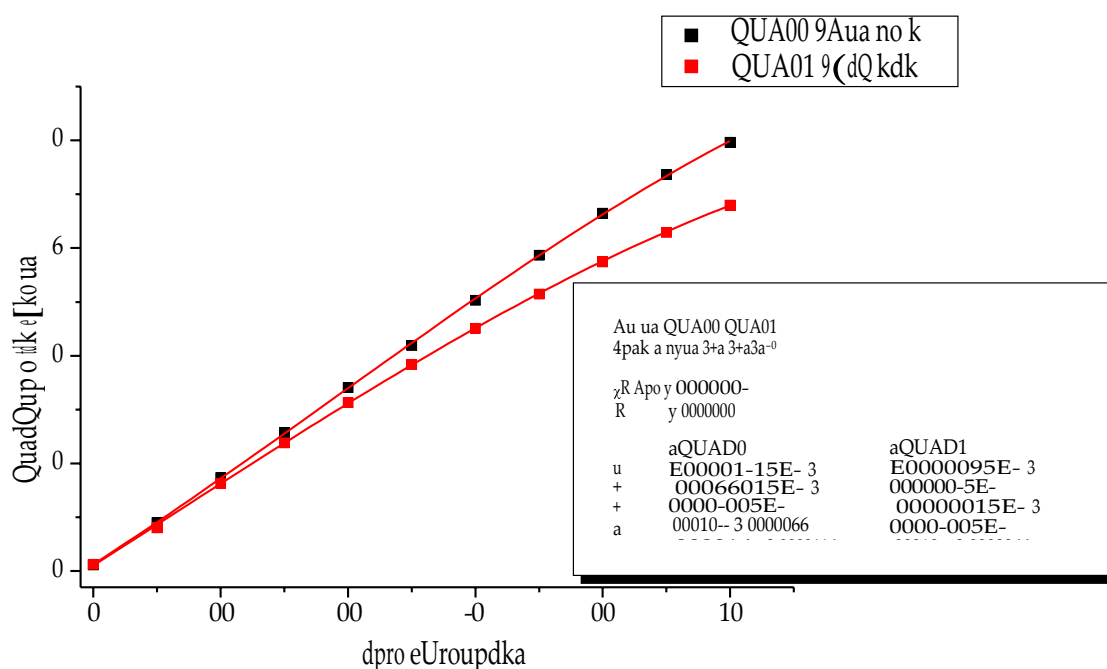


Figure B.1.: Model of quadrupole strength as a function of excitation current - Danfysik QUAD09 compared to Bruker QUAD15

B.1.1. Point-to-point mapping

In order to calibrate the quadrupole QUAD15 in the simplest possible way and to compare it with the model in Figure B.1, the principle of point-to-point mapping (see Figure B.2) was used. From the known distances of the elements as well as the effective length of QUAD15 given in the data sheets, the actual quadrupole strength s was calculated and compared with the model in figure B.1.

The distance between the centre of the wedge and the quadrupole inlet is $L_1^t = 4.37$ m and $L_2^t = 1.70$ m between the quadrupole outlet and the xy monitor. The mechanical length of the quadrupole is $L_{Quad} = 280$ mm, the effective length L_{eff} (abbreviated as l in the following) is however

B.1. simple check of the strength of a quadrupole

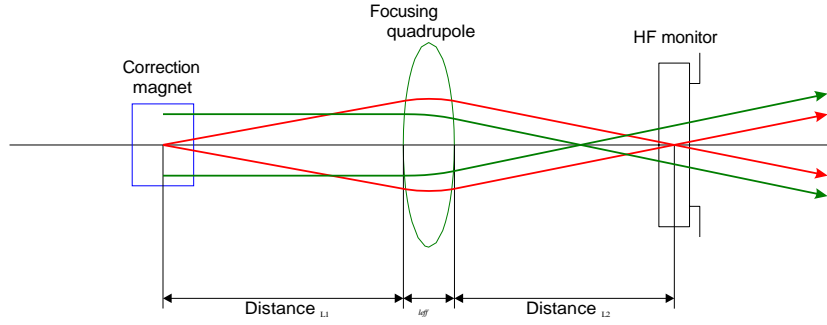


Figure B.2.: Point-to-point imaging with focusing quadrupole

296 mm; this difference must be accounted for the effective drift distances L_1 and L_2 . The transfer matrix thus consists of three elements: a drift path, a quadrupole and a second drift path:

$$m = \begin{pmatrix} 1 & L_2 \\ 0 & 1 \end{pmatrix} \begin{pmatrix} \cos(\sqrt{k-l}) & \sin(\sqrt{k-l}) \\ -\sin(\sqrt{k-l}) & \cos(\sqrt{k-l}) \end{pmatrix} \begin{pmatrix} 1 & L_1 \\ 0 & 1 \end{pmatrix} \quad (\text{B.1})$$

Now point-to-point mapping means that the beam *direction* at the beginning of the system can be chosen arbitrarily without influencing the beam *location* at the exit of the system.¹ This means that the matrix element $m_{12} = 0$ must be valid.

For this purpose, WEDL14 continuously changed its deflection angle in the horizontal direction. During this process, the excitation current was determined manually, at which no beam movement could be detected in XYMO15. The result of these measurements and those carried out at various other steel energies is shown in figure B.3.

In order to determine the effect of the hysteresis, the current was set once from 0 A for each energy and in a second pass from the maximum current of 50 A.

The advantage of this point-to-point mapping is that this method is completely independent of the deflection angle caused by the wedler and, in addition, no calibration of the xy monitor is necessary.

Table B.1.: List of the quadrupole strengths with the corresponding excitation current for point-to-point mapping as well as the corresponding quadrupole strengths of the model $s(i)$ with their deviation from the measurement.

Energy	Current [A]	Measurement [T]	$s(i)$ [T]	Deviation
420 MeV	6.46...7.22	1.110	$1.130 \pm 3.8\%$	1.8 %
495 MeV	7.70...8.54	1.303	$1.319 \pm 3.7\%$	1.2 %
615 MeV	9.68...10.50	1.626	$1.599 \pm 3.7\%$	-1.7 %
855 MeV	13.96...14.86	2.250	$2.215 \pm 3.9\%$	-1.5 %
883 MeV	14.90...15.70	2.334	$2.333 \pm 4.0\%$	0.0 %

¹O. B. d. A. the location at both the input and the output of the system is identically zero.

B. Quadrupole

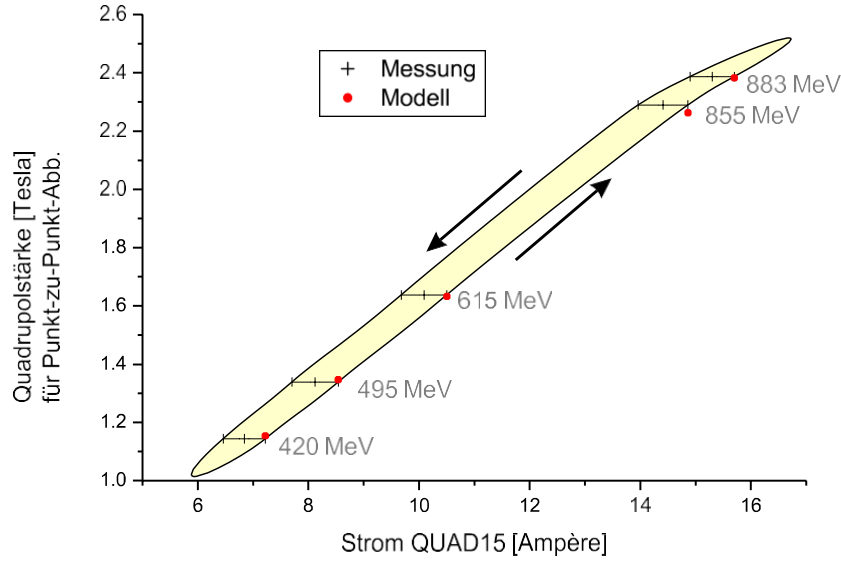


Figure B.3.: Quadrupole strength measured from point-to-point mapping as a function of the excitation current. An effective length of $l_{eff} = 296$ mm from the data sheets was used as a basis.

Quadrupoldates

Table B.2 shows the coefficients for determining the quadrupole strength.

$$s(i) = g(i) - l = \frac{\partial B_x(i)}{\partial z} - l \quad (B.2)$$

according to equation B.3 (the Indian "0" is to indicate that the quadrupole strength is to be reproduced from the switched-off state).

$$s(i) = a - i^3 + b - i^2 + c - i + d \quad (B.3)$$

The red points shown in figure B.3 are the quadrupole strengths calculated from the model $s(i)$ (equation B.4). Since the quadrupole is always driven to its current value from the switched-off state during operation, this model was adjusted by a multiplicative factor in order to be able to describe the position of the points as well as possible by the *lower* hysteresis curve:

$$\underline{s}(i) = s(i) - 0.94 \quad (B.4)$$

However, this investigation of the quadrupole strength would also have to be carried out for the other quadrupoles. Only then can it be decided with certainty whether this correction has statistical or systematic causes.

B.1. simple check of the strength of a quadrupole

Table B.2.: List of the coefficients for determination of the quadrupole strength according to
 $s(i) = a - i^3 + b - i^2 + c - i + d$

Quad	Ser.no.	a	b	c	d
QUAD07	89333	-0.01158E-3 $\pm 0.002E-3$	0.65596E-3 $\pm 0.140E-3$	0.14675 ± 0.003	0.11986 ± 0.016
QUAD08	89335	-0.00768E-3 $\pm 0.002E-3$	0.36418E-3 $\pm 0.140E-3$	0.15409 ± 0.003	0.05934 ± 0.016
QUAD09	89348	-0.01509E-3 $\pm 0.002E-3$	0.85364E-3 $\pm 0.140E-3$	0.14703 ± 0.003	0.1194 ± 0.016
QUAD10	612 2000/13	-0.00567E-3 $\pm 0.002E-3$	-0.17044E-3 $\pm 0.192E-3$	0.17884 ± 0.004	0.11627 ± 0.022
QUAD11	89336	-0.01176E-3 $\pm 0.002E-3$	0.62542E-3 $\pm 0.140E-3$	0.15177 ± 0.003	0.07267 ± 0.016
QUAD12	612 2000/14	-0.00847E-3 $\pm 0.007E-3$	0.00830E-3 $\pm 0.177E-3$	0.17476 ± 0.04	0.11292 ± 0.019
QUAD13	612 2000/15	-0.00678E-3 $\pm 0.007E-3$	-0.19171E-3 $\pm 0.175E-3$	0.17991 ± 0.004	0.11473 ± 0.019
QUAD14	612 2000/10	-0.00919E-3 $\pm 0.006E-3$	-0.03330E-3 $\pm 0.162E-3$	0.17810 ± 0.003	0.10743 ± 0.018
QUAD15	612 2000/8	-0.01107E-3 $\pm 0.004E-3$	0.13075E-3 $\pm 0.248E-3$	0.17386 ± 0.005	0.11366 ± 0.028

C. Theory of HF monitors (by H. Herminghaus)

The following section is taken from the Herminghaus lecture in the summer semester of 1978 [Her78].

C.1. Fields in cylindrical waveguides

Both the beam pipes and the RF monitors are cylindrical objects. Therefore, cylindrical coordinates are suitable for describing the field configurations. Then the solutions of Maxwell's equations can be expressed in the form

$$F(r, \vartheta, z, t) = f_1(r) \cdot f_2(\vartheta) \cdot f_3(z) \cdot f_4(t)$$

be separated.

Two general types of solutions are contained as concrete solutions: so-called H -waves (i.e. fields with $H_z = 0$) and E -waves ($E_z = 0$). In the following we will only deal with the E -waves, the H -waves can be treated analogously. The general form of the solution is then (let A be an arbitrary amplitude factor with the dimension of a voltage: $E \sim A \cdot k \Rightarrow E$ [V/m] and $B \sim A^k \cdot 2 \Rightarrow B$ [Vs/m²]):

$$E_r = \pm A J_m'(k_r r) \cos(m\vartheta) e^{j(\omega t \mp k_z z)} \quad (C.1)$$

$$E_\vartheta = \mp \frac{A m J_m(k_r r)}{k_r r} \sin(m\vartheta) e^{j(\omega t \mp k_z z)} \quad (C.2)$$

$$E_z = \frac{j A k_z}{k_r} J_m(k_r r) \cos(m\vartheta) e^{j(\omega t \mp k_z z)} \quad (C.3)$$

$$B_r = \frac{A k_z}{k_0} \frac{J_m'(k_r r)}{m r} \sin(m\vartheta) e^{j(\omega t \mp k_z z)} \quad (C.4)$$

$$B_\vartheta = \frac{A}{k_0} \frac{c k_z}{r} J_m'(k_r r) \cos(m\vartheta) e^{j(\omega t \mp k_z z)} \quad (C.5)$$

$$B_z = 0 \quad (C.6)$$

with the separation condition

$$k_z^2 + k_r^2 = k_0^2 \quad (C.7)$$

where the vacuum wave number $k_0 = \frac{2\pi}{\lambda_0} = \frac{\omega}{c}$ is used.

The expression $e^{j(\omega t \mp k_z z)}$ describes the location and time dependence and means that the wave in the case *minus* runs along the *positive* z -axis.

The J_m are the Bessel functions of m th order. Since B_r and E_ϑ must disappear on the metallic waveguide wall, the following relationship follows from equations C.1 to C.6 for a waveguide radius a

$$J_m(k_r a) = 0 \quad (C.8)$$

C.2. Standing waves in resonators

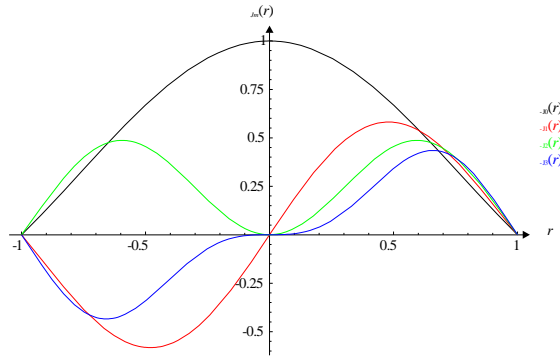


Figure C.1: The Bessel functions $J_m(r)$ describe the field strength $E_z(r)$ in the cylindrical resonator. Condition for conductive surface is $J_m(kra) = 0$, here the functions are shown up to the first zero.

Equation C.8 has an infinite number of solutions for given a and m , however, after Equation C.7 gives the so-called „cutoff“ wavenumber for the respective mode at which wave propagation in the z -direction is still possible. According to equation C.7, k_z approaches zero, when k_r grows. For even smaller frequencies, k_z becomes imaginary and wave propagation is no longer possible, the fields decay exponentially.

The modes of the E -waves are denoted by E_{mn} or TM_{mn} , where in equation C.1 to C.6 m describes the azimuthal behaviour and n as the n th zero of equation C.8 the radial behaviour of the fields.

C.2. Standing waves in resonators

If two waves of the same amplitude travelling in opposite directions are superimposed, a standing wave is obtained. With the same amplitude, the time-dependent part of equations C.1 to C.6 results in

$$e^{j(\omega t - k_z z)} + e^{j(\omega t + k_z z)} = 2 \cos(k_z z) e^{j\omega t} \quad (\text{C.9})$$

For the field components where the sign reverses with the direction of travel, this becomes

$$e^{j(\omega t - k_z z)} - e^{j(\omega t + k_z z)} = -2j \sin(k_z z) e^{j\omega t}$$

(C.10) This results from equations C.1 to C.6

$$E_r = -2jAJ^t (k_r r) \cos(m\vartheta) \sin(k_z z) e^{j\omega t} \quad (C.1t)$$

$$E_\vartheta = \frac{2jAmIm(krr)}{krr} \sin(m\vartheta) \sin(k_z z) e^{j\omega t} \quad (C.2t)$$

$$E_z = \frac{2jAkr}{m r} J(k r) \cos(m\vartheta) \cos(k_z z) e^{j\omega t} \quad (C.3t)$$

$$B_r = 2 \frac{A_{k0} k_z m Im(krr)}{c k k r z r} \sin(m\vartheta) \cos(k_z z) e^{j\omega t} \quad (C.4t)$$

$$B_\vartheta = 2 \frac{A_{k0}}{c k_z} J^t(k r) \cos(m\vartheta) \cos(k_z z) e^{j\omega t} \quad (C.5t)$$

$$B_z = 0 \quad (C.6t)$$

C.3. The relativistic particle in the HF field

For further consideration, we assume particles whose motion along the z-axis is and a transverse deflection can be neglected. "Relativistic" is to be understood in such a way that the velocity of the particles can also be regarded as approximately constant. and thus the time is related to the place in a simple way:

$$t = t_0 + \frac{z}{v} \quad (C.11)$$

The time dependence of the fields takes the following form:

$$E(r, \vartheta, z, t) = E(r, \vartheta, z) e^{j\omega t}$$

(C.12) We further perform a Fourier expansion of the fields along the z-axis:

$$F(r, \vartheta, k_z) = \int_{-\infty}^{+\infty} E(r, \vartheta, z) e^{jk_z z} dz \quad (C.13)$$

with the inversion

$$E(r, \vartheta, z) = \frac{1}{2\pi} \int_{-\infty}^{+\infty} F(r, \vartheta, k_z) e^{-jk_z z} dk_z \quad (C.14)$$

If a particle of charge e passes through a field $E(r, \vartheta, z, t)$ which changes in time, its energy change in electron volts ($E - ds$ is expressed in volts) is as follows

$$\Delta T = \int_s E(r(z), \vartheta(z), z, t(z)) \frac{ds}{dz} dz \quad (C.15)$$

where the trajectory $s(t)$ is described by $r(z)$ and $\vartheta(z)$ and E_I is the tangential field strength to the trajectory. For a particle flying parallel to the z-axis, $r, \vartheta = \text{const}$ and $s \equiv z$. Then equation C.15 becomes

$$\Delta T = \int_s E_z(r, \vartheta, z, t(z)) dz \quad (C.16)$$

With equation C.11 and equation C.12, the energy change becomes

$$\Delta T = e \int_{-\infty}^{+\infty} \int_0^{2\pi} \int_0^{\infty} E_z(r, \vartheta, z) e^{jk_r r} T_z dz \quad (C.17)$$

where k_r is set. Thus k_r is the wave number of a wave whose phase velocity corresponds to the particle velocity v . The phase factor $e^{jk_r r}$ means that the energy gain depends sinusoidally on the phase position of the particle.

Now we consider a particle which reaches a field-permeated space through a beam tube and leaves it again (see figure C.2). The field in the beam tubes is

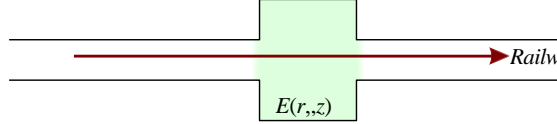


Figure C.2.: Particle flies through resonator

in the „cutoff“ range and thus decays rapidly outside the resonator. The interval for the energy gain extends from $-\infty$ to $+\infty$ and is then as follows

$$\Delta T = e \int_{-\infty}^{+\infty} \int_0^{2\pi} \int_0^{\infty} E_z(r, \vartheta, z) e^{jk_r r} T_z dz = F(r, \vartheta, k_r) \quad (C.18)$$

The particle is therefore only influenced by the spatial Fourier component whose phase velocity coincides with its own particle velocity!

C.4. Rotationally symmetric resonators

Now the case of a rotationally symmetrical resonator of length l , in which a standing wave of *one* mode is supposed to exist, is treated:

$$E(r, \vartheta, z) = S(k_r, r, \vartheta) \frac{e^{jk_l z} + e^{-jk_l z}}{2} \quad (C.19)$$

with $S(k_r, r, \vartheta)$ as the amplitude of the electric field for $z = 0$. S thus also contains the r - and ϑ -dependencies: $S(k_r, r, \vartheta) = A J_m(k_r r) \cos(m\vartheta)$, where of course $k^2 + k_l^2 = k_0^2$ also holds. The

The space filled with fields should extend from $-l/2$ to $+l/2$ (see figure C.3). The case of the re-

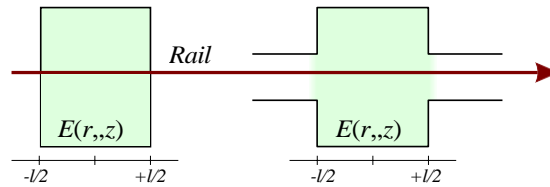


Figure C.3.: Resonator without (left) and with hole (right) in the lid

C. Theory of HF monitors (by H. Herminghaus)

sonator with a hole in the lid can be considered in general: We imagine the field in the cylindrical resonator as an integral over all solutions of Maxwell's equations in cylindrical coordinates. For $k_r = \sqrt{k_0^2 - k_z^2}$:

$$E(r, \vartheta, z) = \int_{-\infty}^{+\infty} A(k_z) J_m(k_r r) \cos(m\vartheta) e^{-jk_z z} dk_z \quad (C.20)$$

If we compare this with the inverse of the Fourier transform from equation C.14, we obtain

$$A(k_z) J_m(k_r r) \cos(m\vartheta) = 2\pi F(r, \vartheta, k_z) \quad (C.21)$$

and from this, again using equation C.18

$$\Delta T = e^{j\omega t} \int_{-\infty}^{+\infty} A(k_z) J_m(k_r r) \cos(m\vartheta) \quad (C.22)$$

Here, the z -integration from $-\infty$ to $+\infty$ also accounts for boundary fields in the resonator tubes.

Now the argument of the Bessel function can be adapted somewhat to our needs:

$$k_r = \sqrt{k_0^2 - k_z^2} = jk_T \sqrt{1 - \left(\frac{k_0}{k_T}\right)^2} = \frac{j\omega}{c} r \sqrt{1 - \beta^2} = \frac{j\omega}{v} \frac{\sqrt{1 - \beta^2}}{\beta} = \frac{jk_0}{\beta\gamma} \quad (C.23)$$

with $\beta = \frac{v}{c}$ and $\gamma = \frac{1}{\sqrt{1 - \beta^2}}$. With one introduces the particle momentum p in units of $m_0 c$ into the

Equation:

$$p = \beta\gamma m_0 c \quad (C.24)$$

and one can further calculate the energy gain with the help of the modified Bessel functions, for the $I_m(x) = J_m(jx)$ applies, transform:

$$\Delta T = e^{j\omega t} \int_{-\infty}^{+\infty} A(k_z) I_m\left(\frac{k_0 r}{\beta\gamma}\right) \quad (C.25)$$

Due to the necessary „cutoff“ in the area of the beam pipe, $k_0 r$ can be of the order of magnitude 1 at the most, which can be seen from the geometric arrangement. This means that the argument of the modified Bessel function for a relativistic particle with $\beta\gamma \gg 1$ small towards 1 and $I_m(x)$ can be developed for small x around 0:

$$\begin{aligned} I_0(x) &\sim 1 + \frac{x^2}{4} \\ I_1(x) &\sim \frac{x}{2} + \frac{x^3}{8} \\ I_2(x) &\sim \frac{x^2}{8} + \frac{x^4}{16} \\ I_3(x) &\sim \frac{x^3}{48} + \frac{x^5}{160} \\ \text{general: } I_m(x) &= \frac{(x/2)^m}{m!} + \frac{(x/2)^{m+2}}{(m+1)!} + \frac{(x/2)^{m+4}}{2(m+2)!} + \frac{(x/2)^{m+6}}{6(m+3)!} + \dots \end{aligned} \quad (C.26)$$

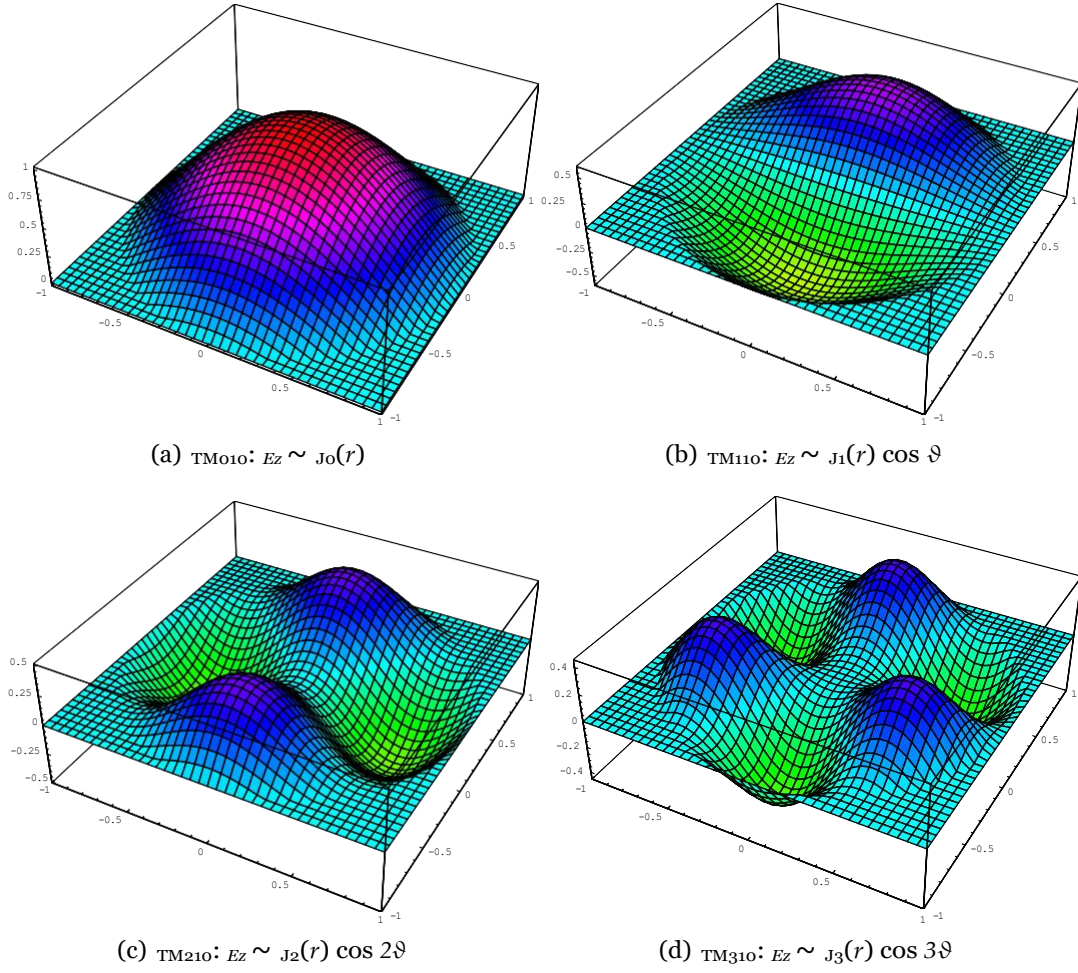


Figure C.4.: Field distributions $E_z(r, \vartheta)$ in the cylindrical resonator; only *one* of the solutions (cosine) is shown. The same colour tone means the same field strength. The antennas are located at position (0,0.481) - this is where E_z of the TM_{110} mode is largest.

C. Theory of HF monitors (by H. Herminghaus)

Substituting this approach into equation C.25, one finally obtains the energy gain for the first modes

$$\Delta T \sim e \int_0^{j\omega t} A(k) i \left(1 + \frac{1}{4} \frac{k_0 r}{\beta \gamma} \right)^2 l \quad \text{for } m = 0$$

$$B(k_T) k_0 r \left(1 + \frac{1}{8} \frac{k_0 r}{\beta \gamma} \right)^2 \cos \vartheta \quad \text{for } m = 1$$

$$C(k_T) (k_0 r)^2 \left(1 + \frac{1}{16} \frac{k_0 r}{\beta \gamma} \right)^2 \cos 2\vartheta \quad \text{for } m = 2 \quad (C.27)$$

$$D(k_T) (k_0 r)^3 \left(1 + \frac{1}{16} \frac{k_0 r}{\beta \gamma} \right)^2 \cos 3\vartheta \quad \text{for } m = 3$$

etc.

With increasing momentum, the r -dependence becomes more and more exactly proportional to r^m . Thus two of these cases are particularly interesting in accelerator physics:

1. **The E_0 modes:** $\Delta T \rightarrow \text{const} \cdot r$ (suitable for acceleration sections as well as phase and intensity monitors)
2. **The E_1 modes:** $\Delta T \rightarrow \sim r^2$ (suitable for position monitors)

For electrons at an energy of 855.15 MeV, the value for $\beta \gamma$ is already 1673.48, which already undercuts the next higher-order terms by 7 orders of magnitude (however, non-linearity must be taken into account in the RF monitors until after the injector linac (3.5 MeV)).

List of figures

2.1. Overview of the accelerator facility	9
2.2. Coordinate system.....	10
2.3. Deflecting magnet (schematic)	12
2.4. Field course of DIPL11	13
2.5. Principle in measuring the T2 system.....	14
2.6. Calibration of XYMO15.....	16
2.7. Set with BEAMOPTIK	18
2.8. Determination of the measuring point a^{07} with WEDL07 on XYMO14	20
3.1. Schematic structure of an xy monitor (Schumann type).....	25
3.2. open „high-Q“ position monitor (photo).....	25
3.3. Schematic of the signal processing of an HF monitor	27
3.4. Arrangement for calibrating the measuring electronics (schematic)	27
3.5. Calibration of the measuring electronics.....	28
3.6. Signal of the c.w. beam on Tektronix oscilloscope.....	29
3.7. c.w.-calibration at 3.6 μ A.....	30
3.8. Sensitivity to jet current	31
3.9. Signal of the diagnostic pulse on Tektronix oscilloscope.....	32
3.10. Numerical pulse integration	33
3.11. Diagnostic pulse calibration.....	33
3.12. c.w.-calibration with adjusted reference phases.....	34
3.13. Course of the linear and cubic fractions ($\sim x$ and $\sim x^3$).....	35
4.1. Schematic of the XYMO14 frame before and after installation of the lifting mechanism	38
4.2. Swash plate (principle)	39
4.3. Movement of the xy monitor (principle)	41
4.4. Position calibration of the monitor.....	42
4.5. Transverse forces and axial play	44
4.6. Dimensioning the lifting mechanism	46
4.7. Calibration mechanics in the SFTF (photo)	47
5.1. Positions of the HF monitors including extraction	48
5.2. Diagnostic pulses on the operating oscilloscope (photo)	49
5.3. Pulse triggers and signals (old system).....	49
5.4. Pulse triggers and signals (automatic channel switching only).....	50
5.5. Pulse trigger and signals (automatic switching and triggering)	51
5.6. Jitter of the COBRA trigger	52
5.7. Block diagram of the COBRA system	54
5.8. xy monitors of the SFTF beamline	55

List of figures

A.1. Sketch of a correction magnet	60
A.2. Longitudinal field at 1 ampere	61
A.3. Effect of Wedler „cycling“.....	61
A.4. Deviation of the deflection angle (transverse) at 1 Amp`ere.....	62
A.5. Deflection angle of the duster	63
B.1. Quadrupole strength QUAD09 and QUAD15	64
B.2. Point-to-point mapping.....	65
B.3. Measurement of the quadrupole strength at different energies	66
C.1. Bessel functions $J_m(r)$	69
C.2. Jet pipe and resonator.....	71
C.3. Resonator with and without hole in the lid.....	71
C.4. Field distributions $E_z(r, \vartheta)$ in the cylinder resonator.....	73

List of tables

2.1. List of the fitted quadrupole strengths.....	22
2.2. List of fitted field indices	22
3.1. Beam current sensitivity XYMO14	30
A.1. List of the Wedler data.....	63
B.1. Quadrupole strength list for point-to-point mapping	65
B.2. Quadruple Soldiers' Line-up	67

Bibliography

- [Bro80] K.L. Brown et al.: *TRANSPORT, a computer program for designing charged particle beam transport systems* (also published as SLAC-r-091)
(CERN 80-04, <http://pc102.psi.ch/ftp/CERN-80-04/>)
(SLAC 91-03, <http://www.npl.uiuc.edu/~debevec/mulan/documentation/>)
- [CAS84] CERN Accelerator School: *General Accelerator Physics*, Gif-sur-Yvette, Paris, France 3-14 September 1984 (CERN 85-19)
- [CAS86] CERN Accelerator School: *Second General Accelerator Physics Course*, Scanticon Conference Centre, Aarhus, Denmark 15-26 September 1986 (CERN 87-10)
- [DBG99] Motorola: *dBUG Reference Manual*, Revision 0.21, April 8, 1999, Motorola 1999
- [Dub01] W. Beitz, K.-H. Grote: *Taschenbuch für den Maschinenbau*, 20th ed.
Publisher Berlin 2001
- [Eut98] H. Euteneuer, A. Alimov: *Remarks and Data on the RF Monitors in the MAMI Beamlines*, Internal Note 02/98, Institut für Kernphysik, Universität Mainz, 1998.
- [Gre03] Marc Grewe: *Applications of SVD in Accelerator Physics*, MAMI-Seminar 27.11.2003, Institut für Kernphysik, Universität Mainz, 2003
- [Her78] H. Herminghaus: *Lecture script „Physikalische Prinzipien der Hochfrequenzbeschleuniger“*, Summer Semester 1978, Institut für Kernphysik, Universität Mainz, 1978
- [Kla67] G. Klages: *Einführung in die Mikrowellenphysik (Introduction to Microwave Physics)*, Dr. Dietrich Steinkopf Verlag, Darmstadt 1967.
- [Kre81] Hans-Joachim Kreidel: *Das System zur selbsttätigen Optimierung der Strahlage im Mainzer Mikrotron - seine Entwicklung und Erprobung an der 14 MeV-Stufe*, Diploma thesis,
Institute for Nuclear Physics, University of Mainz, 1981
- [MCF98] Motorola: *ColdFire® 2/2M Integrated Microprocessor User's Manual*,
Motorola 1998
(http://e-www.motorola.com/files/netcomm/doc/ref_manual/COLDFIRE2UM.pdf)
- [Mee03] David Meeker: *Finite Element Method Magnetics - User's Manual*, Version 3.3,
May 24, 2003 (<http://femm.berlios.de>)
- [Mit92] Dietmar Mittwich: *Entwicklung und Erprobung eines Hochfrequenzmonitors zur Messung der Intensität und der Lage eines 855 MeV Elektronenstrahls*, Diploma thesis, Institut für Kernphysik, Universität Mainz, 1992.
- [SLC72] SLAC Report No. 75 Revision 3: *A First- and Second Order Matrix Theory for the Design of Beam Transport Systems and Charged Particle Spectrometers* (Karl L. Brown),
Stanford University, Stanford, California August 1972
(SLAC 75-03, <http://www.npl.uiuc.edu/~debevec/mulan/documentation/>)

- [Shv00] I. Shvedunov: *BeamOptics*, INP/MSU, Moscow, private communications, July 2000.
- [Wil96] K. Wille: *Physics of Particle Accelerators and Synchrotron Radiation Sources*, Teubner Verlag 1996
(<http://www.delta.uni-dortmund.de/BP.html>)